RSC Advances

PAPER

View Article Online
View Journal | View Issue



Cite this: *RSC Adv.*, 2024, **14**, 8583

# Facile sonochemically-assisted bioengineering of titanium dioxide nanoparticles and deciphering their potential in treating breast and lung cancers: biological, molecular, and computational-based investigations†

Nada K. Sedky, ‡[a] Noha Khalil Mahdy,‡[b] Nour M. Abdel-kader,[ac] Manal M. M. Abdelhady,[d] Mohamad Maged,[e] Aya L. Allam,[f] Mohammad Y. Alfaifi,[g] Samir N. Shamma,[h] Hatem A. F. M. Hassan[fi] and Sherif Ashraf Fahmy *[j]

Combining sonochemistry with phytochemistry is a modern trend in the biosynthesis of metallic nanoparticles (NPs), which contributes to the sustainability of chemical processes and minimizes hazardous effects. Herein, titanium dioxide ($TiO_2$) NPs were bioengineered using a novel and facile ultrasound-assisted approach utilizing the greenly extracted essential oil of *Ocimum basilicum*. FTIR and UV-Vis spectrophotometry were used to confirm the formation of $TiO_2$ NPs. The X-ray diffraction (XRD) analysis showed the crystalline nature of $TiO_2$ NPs. TEM analysis revealed the spherical morphology of the NPs with sizes ranging from 5.55 to 13.89 nm. Energy-dispersive X-ray (EDX) confirmed the purity of the greenly synthesized NPs. $TiO_2$ NPs demonstrated outstanding antitumor activity against breast (MCF-7) and lung (A-549) cancer cells with estimated $IC_{50}$ values of 1.73 and 4.79 μg $mL^{-1}$. The $TiO_2$ NPs were cytocompatible to normal cells (MCF-10A) with a selectivity index (SI) of 8.77 for breast and 3.17 for lung cancer. Biological assays revealed a promising potential for $TiO_2$ NPs to induce apoptosis and arrest cells at the sub-G1 phase of the cell cycle phase in both cancer cell lines. Molecular investigations showed the ability of $TiO_2$ NPs to increase apoptotic genes' expression (Bak and Bax) and their profound ability to elevate the expression of apoptotic proteins (caspases 3 and 7). Molecular docking demonstrated strong binding interactions for $TiO_2$ NPs with caspase 3 and EGFR-TK targets. In conclusion, the greenly synthesized $TiO_2$ NPs exhibited potent antitumor activity and mitochondrion-based cell death against breast and lung cancer cell lines while maintaining cytocompatibility against normal cells.

Received 28th December 2023
Accepted 7th March 2024

DOI: 10.1039/d3ra08908h

rsc.li/rsc-advances



## 1. Introduction

Cancer is one of the leading causes of mortality in the world. It poses a burden on societies, healthcare systems, and the quality of human life.[1–3] One in every six deaths is attributed to cancer globally. Breast and lung tumors are at the top of the list as the world's most prevalent cancers.[4,5] Global efforts are needed to find novel chemotherapeutic agents or enhance the efficacy and safety of existing drugs.[5] Some tumors fail to respond to treatment owing to the poor absorption of the chemotherapeutic

[a]*Department of Biochemistry, School of Life and Medical Sciences, University of Hertfordshire Hosted by Global Academic Foundation, R5 New Garden City, New Administrative Capital, Cairo 11835, Egypt*
[b]*Department of Pharmaceutics and Industrial Pharmacy, Faculty of Pharmacy, Cairo University, Kasr El-Aini Street, Cairo 11562, Egypt*
[c]*Department of Biochemistry, Faculty of Science, Ain Shams University, Cairo 11566, Egypt*
[d]*Clinical Pharmacy Department, Faculty of Pharmacy, Badr University, Cairo 11829, Egypt*
[e]*Faculty of Biotechnology, Nile University, Giza, Egypt*
[f]*School of Life and Medical Sciences, University of Hertfordshire Hosted by Global Academic Foundation, New Administrative Capital, Egypt*
[g]*King Khalid University, Faculty of Science, Biology Department, Abha 9004, Saudi Arabia*
[h]*Institute of Global Health and Human Ecology, School of Sciences & Engineering, The American University in Cairo, AUC Avenue, P.O. Box 74, New Cairo 11835, Egypt*
[i]*Department of Pharmaceutics and Industrial Pharmacy, Faculty of Pharmacy, Cairo University, 11562 Cairo, Egypt*
[j]*Department of Chemistry, School of Life and Medical Sciences, University of Hertfordshire Hosted by Global Academic Foundation, R5 New Garden City, New Capital, Cairo 11835, Egypt. E-mail: sheriffahmy@aucegypt.edu; Tel: +20-1222613344*

† Electronic supplementary information (ESI) available. See DOI: https://doi.org/10.1039/d3ra08908h

‡ These authors contributed equally to this work.

drug into the targeted cells[6] or extensive adverse effects on normal cells.[7,8] The advent of nanotechnology paved the way for cancer research to explore more antitumor treatment agents; thanks to the "enhanced permeability and retention" (EPR) phenomenon that enabled the passive targeting of nanosized particles into the tumor cells *via* their leaky distorted vasculature system that is not typically observed in healthy cells.[7,9–11] Nanoparticle delivery systems transport the antitumor drug preferentially into cancer cells due to their extensive blood supply and leaky cell membranes.[8,12] Interestingly, antitumor drugs are retained inside cancer cells because of the restricted lymphatic drainage.[13,14] Metallic nanoparticles, such as Ag, Au, Cu, Zn, Ti and Pt NPs antineoplastic agents due to their inert behavior towards normal cells, yet selective-targeting to the leaky cancer membranes.[7,15–17] Thus, their application as potentially effective yet safe anticancer agents has drawn much attention recently.[18]

In particular, titanium dioxide nanoparticles ($TiO_2$ NPs) have shown valuable applicability in various fields, including cosmetics, sericulture, wastewater remediation, air purification, and the food industry.[19] Smart improvements in their synthesis and formulation were necessary to overcome some of their chemical instability in aqueous solutions.[20] $TiO_2$ NPs have distinguished properties relevant to other metals. Besides, $TiO_2$ NPs have promising biomedical applications in treating bacterial and viral infections. In addition, $TiO_2$ NPs were tested as nanocarriers for several antitumor drugs.[21,22] But not until recently they were shown to serve as potential antitumor agents by themselves against solid cancers.[23] $TiO_2$ NPs rose as promising candidates in the antitumor arsenal due to their remarkable surface properties, chemical stability, biocompatibility, and biological anti-proliferative activity,[15] as compared to other metallic NPs. Several chemical methods have been utilized to synthesize different metallic NPs. However, these methods involve toxic solvents with several perilous environmental and human health implications.[24] Thus, numerous green approaches have been developed for synthesizing various metallic NPs and were considered a breakthrough in enhancing the activity of metallic NPs while minimizing toxicity and environmentally hazardous effects.[14] Green synthesis entails using plant extracts or microorganisms rather than harsh chemicals. These eco-friendly methods are biocompatible, preventive to unnecessary wastes, cost-effective, and safe for the environment and humans.[25] It relies on various phytochemicals, such as polysaccharides, terpenoids, organic acids, proteins *etc.*,[26] to reduce metallic atoms, converting them into nanoscale counterparts (bottom-up approach).[25,27,28] In addition, natural compounds aid in stabilizing the metallic NPs and enhancing their surface properties.[24,29]

*Ocimum basilicum*, basil, is a well-known herb that possesses numerous potential medicinal and biotechnological applications. Natural ingredients extracted from basil were reported to have antibacterial and anticancer activities.[27,30–33] Some efforts were committed to synthesizing metal nanoparticles using basil herbal extract. However, to the best of our knowledge, no studies in the literature reported the biofabrication of anticancer $TiO_2$ NPs using basil essential oils.[30,34] Most of the previous studies focused on the antibacterial activity[35,36] rather than the antitumor effect of basil-mediated-$TiO_2$ NPs.

In this study, we designed a novel eco-friendly $TiO_2$ NPs using a greenly extracted essential oil of *O. basilicum*. The greenly engineered NPs were characterized physicochemically using various techniques, including spectroscopic techniques, X-ray diffraction, transmission electron microscopy, scanning Electron Microscopy (SEM), and Energy-Dispersive X-ray (EDX). The greenly synthesized nanoparticles were then evaluated for their biological activity using a comprehensive panel of cellular biology, bioinformatics, cytogenetics, molecular biology, and molecular docking techniques. Several assays were performed, including apoptosis, cell cycle analysis, gene expression analysis, and western blotting, to examine the underlying molecular mechanisms of our green $TiO_2$ NPs-induced cell death in both tumor models. In addition, a molecular docking study was conducted to predict the binding interactions of $TiO_2$ NPs with two of the most well-known targets in both breast and lung tumors: caspase 3 and EGFR-TK.

## 2. Methods

### 2.1. Green extraction and characterization of *Ocimum basilicum* essential oil (OBO)

OBO was extracted using a green method by hydrodistillating the aerial parts of *O. basilicum* L. locally grown in Greece, at the whole flowering stage, utilizing a Clevenger-type apparatus. Hydrodistillation was carried out by adding 250 g of fresh plant material to 1 L of distilled water. The hydrodistillation took place at 110 °C, which was then reduced to 80 °C, keeping the cooling system's temperature at 4 °C. The obtained OBO was then stored in firmly closed amber glass bottles at 4 °C for further experiments. The chemical components of the extracted oil were analyzed using GC-MS (Agilent Technologies gas chromatography (7890B) and a mass spectrometer detector (5977B)), as detailed in our previous studies.[14,37]

### 2.2. Sonochemical green synthesis of $TiO_2$ NPs

Eco-friendly $TiO_2$ NPs were synthesized by reducing titanium(I) isopropoxide using OBO and sonochemical reaction. In brief, 5 mL of OBO was added to 15 mL of titanium(I) isopropoxide solution (10 mM) while being ultrasound irradiated using an ultrasonic homogenizer (Pulse 150 Benchmark, USA) for 15 min. A horn of 21 kHz frequency was placed centrally at 1 cm depth of the mixture with an optimum sonication amplitude of 40%. The obtained $TiO_2$ NPs were purified by ultracentrifugation for 30 min at 12 000 rpm, and the remaining pellet was washed thrice with deionized water to remove any plant residual materials. The final pellet was resuspended in deionized water and then subjected to freeze drying for 24 h.

### 2.3. Characterization of the eco-friendly $TiO_2$ NPs

**2.3.1. Spectroscopic techniques.** The prepared $TiO_2$ NPs were characterized using a dual beam UV-Vis spectrophotometer (Peak Instruments T-9200, USA), and the chemical features of the NPs were studied using FTIR spectroscopy (vertex 70 RAM II, Bruker Spectrometer).

**2.3.2. X-ray diffraction (XRD).** The XRD pattern of the prepared $TiO_2$ NPs was obtained using XPERT-PRO Powder Diffractometer system. The Cu Kα radiation wavelength used was $\lambda = 1.54614°$. The diffractograms were acquired at a $2\theta$ step size of 0.001° and a $2\theta$ range of 20° - 80° for phase identification. The average particle size of $TiO_2$ NPs was calculated by the application of the Debye–Scherrer equation:

$$D = \frac{k\lambda}{\beta \cos \theta}$$

In this equation, $D$ is the crystallite diameter (nm), $k$ is the Scherrer constant and is equal to 0.9, $\lambda$ is the X-ray Cu Kα radiation wavelength (°), $\theta$ is the peak position (radians), and $\beta$ is the full width at half-maximum (radians).[38]

**2.3.3. Structural analysis.** The collective surface morphology of the prepared $TiO_2$ NPs was investigated and visualized using a scanning electron microscope (Quanta FEG250-FEI-USA). The surface morphology of the $TiO_2$ NPs was examined *via* a magnification software suite with SEM. The scanning electron microscope setup was fitted with an Energy-Dispersive X-ray (EDAX Genesis APEX 2i with the ApolloX SDD spectrometer) to analyze the elements present in the sample.

**2.3.4. Morphological analysis.** TEM was used to obtain images of individual $TiO_2$ NPs, thus visualizing the morphology of the $TiO_2$ NPs and measuring their average nanoparticle diameter. The sample was imaged using a JEOL-JEM 2100 transmission electron microscope (Musashino, Akishima, Tokyo, Japan). In addition, the selected area electron diffraction (SAED) pattern was obtained. The nanoparticle diameters were measured *via* ImageJ's image processing software (NIH, Bethesda, MD, USA). A nanoparticle diameter histogram was drawn using OriginPro software (OriginLab, OriginPro 8.5, USA), based on 100 measurements.

### 2.4. Cell culture

Human A-549 (lung cancer) and MCF-7 (Breast Adenocarcinoma) were used as cancer models, while the control used was MCF-10A (normal breast epithelium). Cell lines were provided by the American type of culture collection (ATCC, Wesel, Germany). Corresponding cells were cultured in standard DMEM media containing 100 units per mL penicillin and 100 mg $mL^{-1}$ streptomycin. The media was supplemented with10% heat-inactivated fetal bovine serum. Incubation was done at a humidified 5% (v/v) $CO_2$ atmosphere, and the temperature was set to 37 °C.

### 2.5. Cell viability assay

Cell viability assay was done using the specified SRB approach.[39] 100 μL cell suspension aliquots containing ($5 \times 10^3$ cells) were placed in 96-well plates and grown in the designated media for 24 hours. Treated cells were exposed to 100 μL media containing $TiO_2$ NPs at different concentrations (0.03, 0.3, 3, 30, 300 μg $mL^{-1}$). Following 48 hours of drug exposure, cell fixation was routinely done by substituting the media with 150 μL 10% TCA and incubating for 1 hour at 4 °C. Then TCA solution was aspirated, and cells were washed 5 times with distilled water. A 70 μL aliquots of SRB solution (0.4% w/v) were put and incubated in the dark for 10 min at ambient room temperature. Wells were washed with 1% acetic acid 3 times and left to air-dry overnight. To dissolve protein-bound SRB stain, 150 μL of 10 mM TRIS was accordingly added; BMGLABTECH®-FLUOstar Omega microplate reader (Ortenberg, Germany) set at 540 nm was used to measure absorbance.

### 2.6. Apoptosis

Annexin V-FITC apoptosis detection kit (Abcam Inc., Cambridge Science Park, Cambridge, UK), was used to calculate apoptosis or necrosis cell populations according to the recommended protocol. Measurements were recorded using 2 fluorescent-channels flow cytometry. $TiO_2$ NPs treatment was completed at the defined $IC_{50}$ concentrations for 48 hours, followed by cells ($10^5$ cells) collection. Routine trypsinization was done to loosen up cells, followed by washing with ice-cold PBS (pH 7.4) 2 times. Then, 0.5 mL of Annexin V-FITC/PI solution was added to the cells and incubated in the dark for 30 minutes according to the manufacturer's protocol. Cells were stained and then injected *via* ACEA Novocyte™ flowcytometer (ACEA Biosciences Inc., San Diego, CA, USA). FITC and PI fluorescent signals were analyzed ($\lambda_{ex/em}$ 488/530 nm for FITC and $\lambda_{ex/em}$ 535/617 nm for PI, respectively) using FL1 and FL2 signal detector. An estimate of 12 000 events, for each sample, were captured. Quantification of positive FITC and/or PI cells was achieved by quadrant analysis and estimated by ACEA NovoExpress™ software (ACEA Biosciences Inc., San Diego, CA, USA).

### 2.7. Cell cycle analysis

MCF-7 and A-549 cell lines were treated with $TiO_2$ NPs at the determined $IC_{50}$s for 48 hours, $10^5$ cells were harvested for routine trypsinization. Washing was done twice with ice-cold PBS (pH 7.4). Resuspension of cells was achieved by adding 2 mL 60% ice-cold ethanol. Cell's fixation was done by incubation for 1 hour at 4 °C. Then, washing of fixed cells was done using PBS (pH 7.4) twice and eventually resuspended in 1 mL solution (PBS pH 7.4 containing 10 μg $mL^{-1}$ propidium iodide (PI) and 50 μg $mL^{-1}$ RNAase A). Incubation was done at 37 °C for 20 minutes. Flow cytometry was used to analyze DNA content by FL2 ($\lambda_{ex/em}$ 535/617 nm) signal detector (ACEA Novocyte™ flow cytometer, ACEA Biosciences Inc., San Diego, CA, USA). An estimate of 12 000 events, per sample were acquired. ACEA NovoExpress™ software (ACEA Biosciences Inc., San Diego, CA, USA) was eventually used to evaluate cell cycle distribution.

### 2.8. Gene selection based on bioinformatics' analysis

**2.8.1. Data processing.** The RNA-Seq data and clinical information of TCGA-BRCA and TCGA-LUSC were downloaded from the TCGA database (**https://portal.gdc.cancer.gov/**), a by the TCGAbiolinks R package. Only primary solid tumor and solid tissue normal samples were retained in both datasets. The data has been preprocessed by removing genes with null expression in over 50% of samples. In addition, the genes with zero variance across all samples were excluded. The Ensembl IDs were mapped to their corresponding HUGO

Gene Nomenclature Committee (HGNC) symbol(s) using the mapping file available from TCGA database. Expression of genes mapping values to multiple Ensembl IDs was averaged across all the samples to avoid redundancy. DESeq2 will use the median of ratios method to perform normalization preprocessing on the input raw read counts data.

**2.8.2. Differentially expressed gene (DEG) analysis.** Differentially expressed genes (DEGs) were identified between the tumor and normal samples using $|\log_2 FC| > 0.1$ and adj-$p < 0.05$ in the DESeq2 R package.

### 2.9. Gene expression for apoptotic markers

Total cellular RNA was extracted using the QIA amp Viral RNA Mini Kit (Qiagen, Hilden, Germany) as per the manufacturer's guidelines. ReverAid RT Kit purchased from (ThermoFisher Scientific, Waltham, USA) and Bio-Rad™ 100 thermal cycler were used to reverse transcribe the isolated RNA according to the kit's protocol. 1 μL of cDNA collected from each sample was assayed afterwards by quantitative real-time PCR (RT-qPCR) for the target genes, BAX, BAK and the housekeeping β-actin gene. The primers' sequences used in this study for the RT-qPCR analysis are reported in Table S1.† The assay was done on a "Rotor-Gene Q-Qiagen Real-time PCR thermal cycler" using the standard conditions. The resulting data were normalized to the control β-actin, and the relative normalized gene expression output was measured by the $2^{-\Delta\Delta C_t}$ approach.[40]

### 2.10. Immunoblotting for apoptotic proteins

Western blot analysis was deployed to determine the relative quantity of caspase-3 and caspase-7 proteins in the cells treated with $TiO_2$ NPs as compared to untreated cells (control). The β-actin protein was chosen for data normalization. Briefly, MCF-7 cells were scraped off the plate using a cold, sterile cell scraper and transferred into a pre-cooled microcentrifuge tube where agitation was performed for 30 min at 4 °C. Whenever necessary, cells were sonicated 3 times for 10–15 s to complete cell lysis. The cellular solution was then spun at 16 000*g* for 20 min in a 4 °C pre-cooled centrifuge. The supernatant was translocated to a fresh tube while the pellet was discarded. A small volume (20 μL) of our lysate was allocated to the protein assay. The protein concentration was measured for each cell lysate. The 2× Laemmli sample buffer was then added at an equal volume to that of the sample and heated to 95 °C for 5 min. This was followed by a centrifugation step at 16 000*g* in a microcentrifuge for 1 min. At this moment, the samples were prepared and ready to be loaded into the SDS (mini SDS-PAGE gel), where equal amounts of protein (25 μg) were loaded into the wells, along with molecular weight markers (Thermo-Scientific PageRuler Broad Range Unstained Protein Ladder, Cat #: 26630). The gel was left to run for 5 min at 90 V, then the voltage was increased to 100–150 V to speed up the run. Directly afterwards, the gel was placed in 1× transfer buffer for 10–15 min. The transfer sandwich was then prepared, ensuring no air bubbles entered the assembly. The blot was allocated to the cathode, and the gel was placed at the anode. The cassette was moved to the transfer tank containing ice blocks. Accordingly, the protein was transferred from the gel to the membrane. The sample was blocked in 3% bovine serum albumin (BSA) in Tris-buffered saline with Tween 20 (TBST) buffer at room temperature for 1 h. The samples were incubated with the primary antibodies against the target proteins (Table S2†) overnight at 4 °C. The blot was then washed 3–5 times for 5 min with TBST and incubated with HRP-conjugated secondary antibodies (Table S2†) for 1 h at room temperature. The blot was then rinsed 3–5 times for 5 min with TBST. According to the manufacturer's guidelines, the chemiluminescent reaction was done using the ECL western blot HRP substrate (Pierce, Thermo-Fisher Scientific). The chemiluminescent signals were captured using the ChemiDoc imaging system of Bio-Rad. This software was also used in the densitometry calculations.

### 2.11. Molecular docking

Titanium dioxide NPs ($TiO_2$ NPs) activity against cell proliferation and molecular pro-apoptotic activity was tested *in silico* by

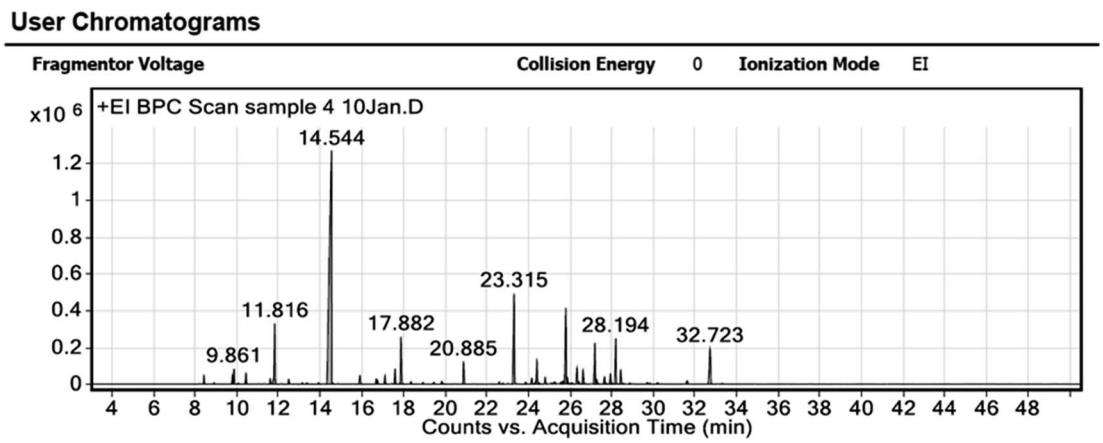


Fig. 1 The GC-MS chromatogram of the extracted *Ocimum basilicum* oil.

predicting its ability to activate the caspase cascade of A-549 and MCF-7 cancer cell lines upon binding with caspase-3. The X-ray crystallography derived caspase-3 (CAS329306) in complex with 4-methyl-benzenesulfonamide (MB) was obtained from Protein Data Bank (PDB ID: 2XYG; http://www.rcsb.org/structure/2XYG).[41] GFR-tyrosine kinases (EGFR-TK) were also chosen as a vital receptor in triggering and generating signaling reactions for both cell lung cancer (CLC) and breast cancer (BC) (PDB ID: 1M17; http://www.rcsb.org/structure/1M17).[42,43]

Water molecules in the 2 crystal structures were deleted using AutoDock tools, and polar hydrogen atoms were added. Marsili–Gasteiger partial charges are appointed employing a two-phase algorithm. The receptor crystal structures were subjected to energy minimization using the AutoDockTools (ADT, v1.5.6) prepare_receptor4.py command, where Kollman-united charge was used for calculating the partial atomic charge.

The structure of $TiO_2$ was drawn using ChemSketch, and its geometry was optimized by Autodock 4.2. To determine the preferred binding sites on crystal structure, the grid box center was set to ($x = 36.357$, $y = 38.829$, $z = 32.088$) and ($x = 20.091$, $y = -1.872$, $z = 58.436$) for PDB IDs 2XYG and 1M17, respectively. The output from AutoDock was further analyzed with UCSF Chimera and PyMOL software package.[44]

### 2.12. Statistical analysis

Data analysis and visualization were accomplished with the aid of GraphPad Prism 6. All the included assays were performed in triplicates. Accordingly, the results are presented as the mean of three individual runs ± standard deviation (SD). The Shapiro–Wilk Test was performed to ensure the normal distribution of the data obtained. Regarding the comparisons of the two groups, a Student's *t*-test was used. As per the comparisons that include three or more groups, ANOVA with multiple comparisons post hoc test was used. Statistical significance is considered at *P*-value $\leq 0.05$.

## 3. Results and discussion

Breast and lung cancers are two leading causes of death globally.[4] Together, they account for 30% of total cancer deaths.[1] In addition, the lung is a very likely site for breast cancer metastasis.[45] Thus, there is a pressing need to develop eco-friendly antitumor agents that can target breast and lung cancers using facile green approaches. In this regard, we greenly synthesized OBO-mediated $TiO_2$ nanoparticles using a sonochemical approach. OBO is prosperous with several bioreductants and capping agents, as evident from the GC-LC analysis, thus, it was exploited for the one-step facile green synthesis of $TiO_2$ NPs with the help of ultrasonic waves.[31,46–48]

### 3.1. Chemical analysis of the extracted OBO using gas chromatography-mass spectrometry (GC-MS)

The GC-MS chromatogram of the greenly extracted OBO is presented in Fig. 1, showing the presence of 58 compounds. The mass spectra of the constituents are listed in Table 1 after being identified with the National Institute of Standards and Technology (NIST) library. Linalool, a monoterpenoid, was recognized as the major component (46.55%) of the analyzed oil. Eugenol, a phenylpropanoid (8.27%), *cis*-α-bergamotene, a bicyclic sesquiterpenoid (6.25%); and Eucalyptol,

Table 1 Chemical composition of the extracted *Ocimum basilicum* oil

| Peak | RT | Compound | Area sum (%) |
|---|---|---|---|
| 1 | 8.413 | α-Pinene | 0.51 |
| 2 | 8.897 | Camphene | 0.07 |
| 3 | 9.782 | Sabinene | 0.51 |
| 4 | 9.861 | 2-β-Pinene | 1 |
| 5 | 10.07 | 1-Octen-3-ol | 0.06 |
| 6 | 10.433 | β-Myrcene | 0.72 |
| 7 | 11.597 | *p*-Cymene | 0.37 |
| 8 | 11.816 | Eucalyptol | 4.53 |
| 9 | 12.486 | β-Ocimene | 0.33 |
| 10 | 13.138 | *cis*-Sabinene hydrate | 0.09 |
| 11 | 13.348 | Linalool oxide B | 0.11 |
| 12 | 13.93 | α-Terpineol | 0.12 |
| 13 | 14.544 | Linalool | 46.55 |
| 14 | 14.609 | Hotrienol | 0.05 |
| 15 | 15.908 | 2-Bornanone | 0.72 |
| 16 | 16.695 | *endo*-Borneol | 0.38 |
| 17 | 16.751 | α-Terpineol | 0.25 |
| 18 | 17.114 | Terpinen-4-OL | 0.6 |
| 19 | 17.598 | L-α-Terpineol | 1.11 |
| 20 | 17.882 | Estragole | 3.44 |
| 21 | 18.361 | *n*-Octyl acetate | 0.16 |
| 22 | 18.934 | β-Citronellol | 0.1 |
| 23 | 19.446 | Carvone | 0.13 |
| 24 | 19.842 | *cis*-Geraniol | 0.22 |
| 25 | 20.885 | Iso-bornyl acetate | 1.66 |
| 26 | 22.602 | Elixene | 0.13 |
| 28 | 23.315 | Eugenol | 8.27 |
| 29 | 23.873 | α-Cubebene | 0.15 |
| 30 | 24.162 | (−)-β-Bourbonene | 0.49 |
| 31 | 24.409 | β-Elemene | 1.8 |
| 32 | 24.52 | α-Copaene | 0.08 |
| 33 | 24.8 | Methyleugenol | 0.42 |
| 34 | 25.121 | *trans*-Sesquisabinene hydrate | 0.06 |
| 35 | 25.261 | Isocaryophillene | 0.18 |
| 36 | 25.568 | γ-Muurolene | 0.12 |
| 37 | 25.652 | β-Gurjunene | 0.2 |
| 38 | 25.796 | *cis*-α-Bergamotene | 6.2 |
| 39 | 25.875 | α-Guaiene | 0.44 |
| 40 | 25.992 | (+)-β-Funebrene | 0.06 |
| 42 | 26.331 | Humulene | 1.25 |
| 43 | 26.42 | *cis*-β-Farnesene | 0.17 |
| 44 | 26.625 | (+)-*epi*-Bicyclosesquiphellandrene | 1.09 |
| 45 | 27.193 | Germacrene-D | 3.24 |
| 46 | 27.281 | *cis*-β-Farnesene | 0.35 |
| 47 | 27.654 | γ-Elemene | 0.64 |
| 48 | 27.938 | δ-Guaiene | 0.83 |
| 49 | 28.194 | γ-Cadinene | 3.55 |
| 50 | 28.436 | *cis*-Calamenene | 1.13 |
| 52 | 28.878 | α-Cadinene | 0.07 |
| 53 | 29.707 | (±)-*trans*-Nerolidol | 0.11 |
| 55 | 30.209 | (+)-Spathulenol | 0.11 |
| 56 | 31.615 | Cubenol | 0.34 |
| 57 | 32.723 | α-Cadinol | 4.41 |
| 58 | 33.305 | α-*epi*-Muurolol | 0.06 |

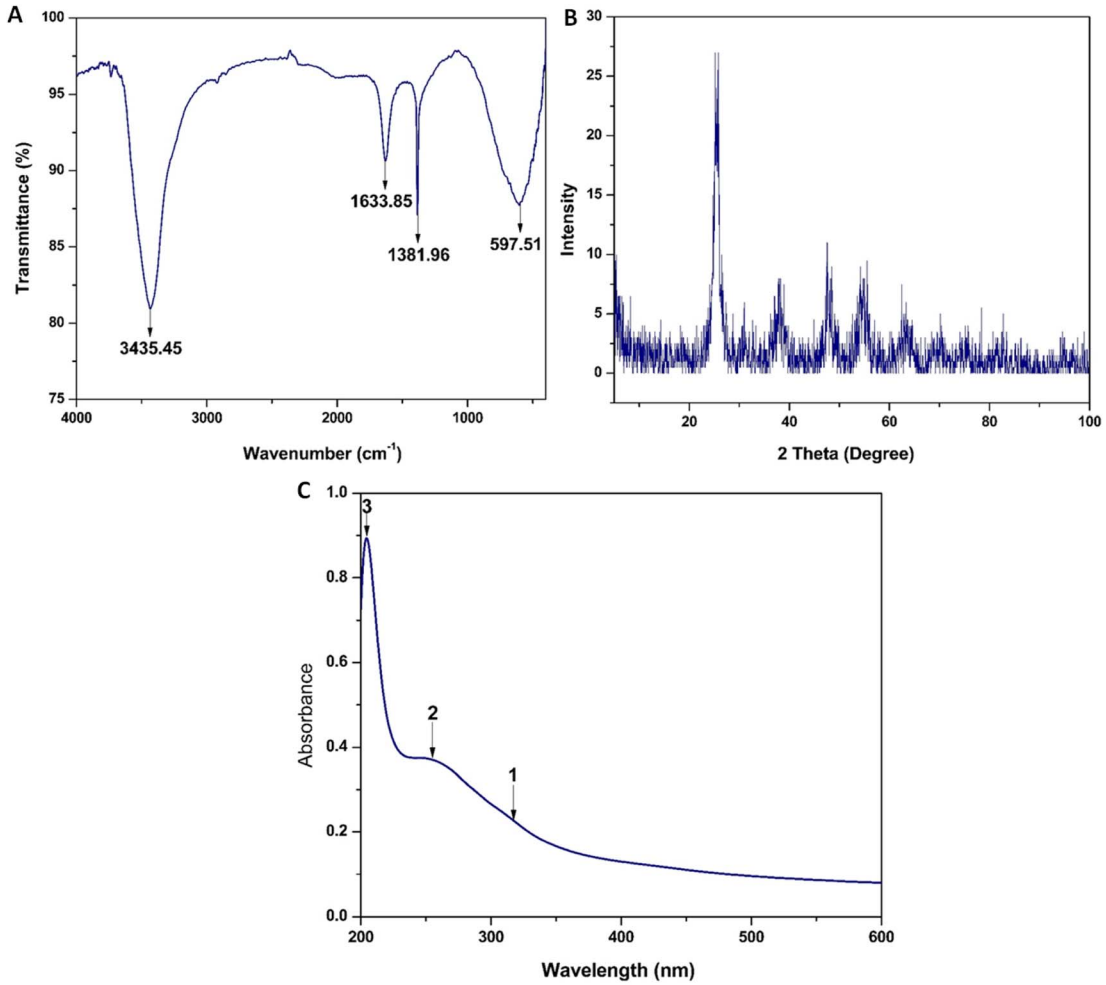


Fig. 2 (A) FTIR spectrum of $TiO_2$ NPs, (B) XRD pattern of $TiO_2$ NPs, and (C) UV-Vis spectrum of $TiO_2$ NPs.

a monoterpenoid (4.53%) were the second, third and fourth most prevalent components, respectively. These compounds were reported to have potent antioxidant activity, and thus, they were the key players in the bioreduction of titanium(I) isopropoxide into $TiO_2$ NPs.[49,50] Moreover, the GC-MS analysis of the extracted *Ocimum basilicum* oil established the presence of other terpene compounds that serve as natural reducing agents. These results are in line with previously reported studies.[51,52]

### 3.2. Characterization of the eco-friendly $TiO_2$ NPs

$TiO_2$ NPs were synthesized using a green and facile method that was environmentally friendly, cheap, and did not involve hazardous reagents. Unlike the chemical methods, our simple method is more effective and benign because of the use of green sonochemical reduction combined with the natural reductants from the greenly extracted OBO to generate the $TiO_2$ NPs. Sonochemical green synthesis is an ultrasound-assisted approach that relies on acoustic cavitation without directly impacting the bond's vibrational energy, resulting in nano-sized particles with high surface area and optimized morphologies and reactivity.[53]

The prepared $TiO_2$ NPs were characterized with regard to their physicochemical properties to confirm the successful synthesis of the crystalline NPs.

**3.2.1. Fourier transform infrared spectroscopy (FTIR).** The FTIR spectrum of the prepared $TiO_2$ NPs is presented in Fig. 2A. Two peaks found at 597.51 $cm^{-1}$ and 1381.96 $cm^{-1}$ can be attributed to the bending vibration of O–Ti–O and the stretching vibration of Ti–O–Ti, respectively. The presence of the Ti–O network confirms the successful formation of the crystalline phase of $TiO_2$.[54,55] Two more peaks were detected at 1633.85 $cm^{-1}$ and 3435.45 $cm^{-1}$ that can be attributed to the bending vibration of –OH group and the stretching vibration of O–H group, respectively. The presence of the hydroxyl group can be associated with the existence of water molecules linked to the surface of $TiO_2$ NPs.[55,56]

**3.2.2. X-ray diffraction (XRD).** The XRD pattern of the prepared $TiO_2$ NPs is presented in Fig. 2B, indicating the crystalline nature of the nanoparticles. XRD peaks of $TiO_2$ crystals were found at 25.3°, 37.7°, 47.5°, 54.9°, 63.7°, 68.7°, 70.6°, and

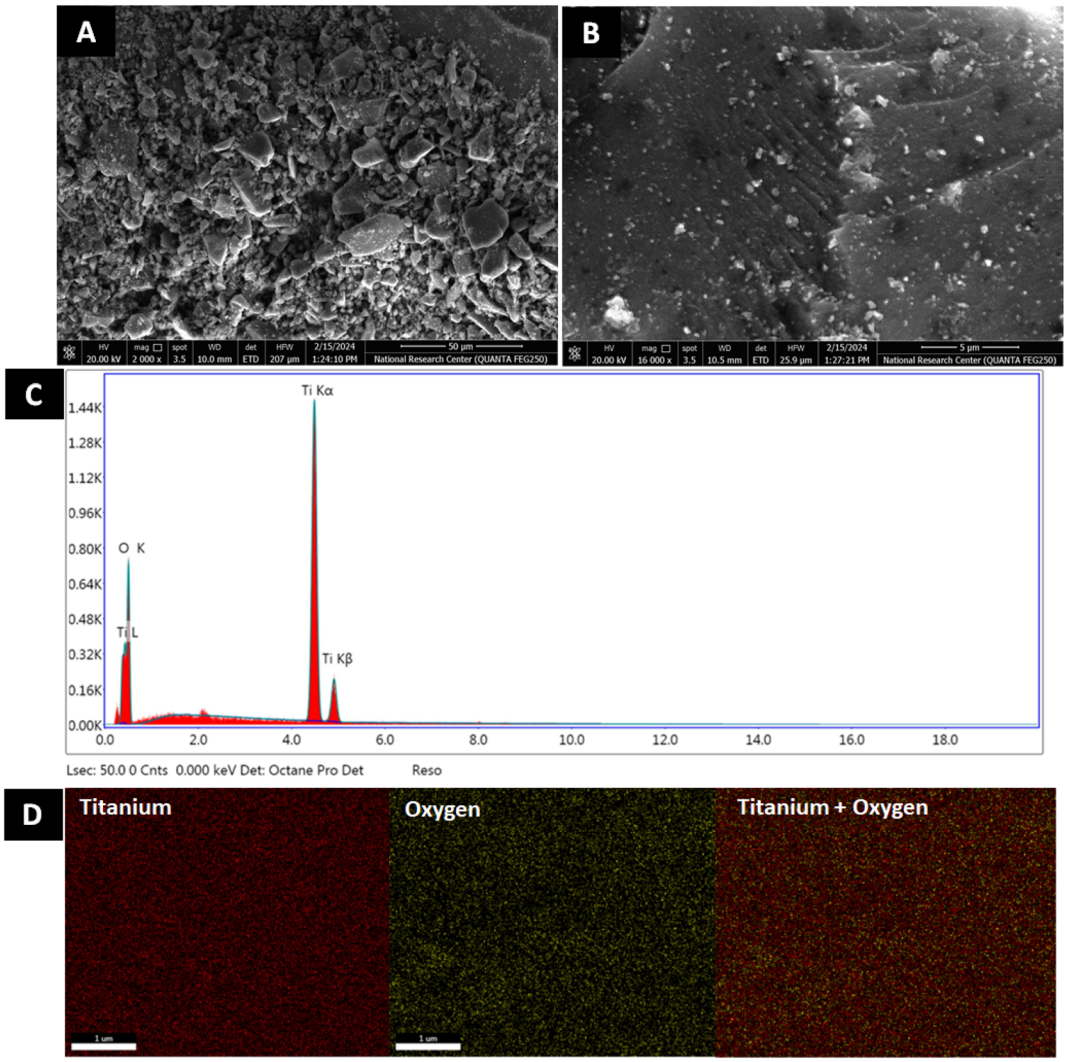


Fig. 3 Morphological and structural analysis of $TiO_2$ NPs. SEM of $TiO_2$ NPs at (A) 50 μm and (B) 5 μm, (C) EDX profile and (D) EDX mapping analysis of $TiO_2$ NPs.

75.5°. The found data are consistent with the inorganic crystal structure database (ICSD) of $TiO_2$ (ICSD card no. 98-001-7737).[57] The absence of impurities in the sample was confirmed by the XRD pattern that showed no excess peaks. $TiO_2$ crystals can be found in different polymorphs, most commonly anatase and rutile. The XRD pattern of the prepared $TiO_2$ NPs showed a major peak at a $2\theta$ of 25.3°, which is attributed to the (110) crystallographic plane found only in $TiO_2$ anatase. This polymorph is generally considered more active than the rutile one.[57,58] The full width at maximum half intensity (FWHM) was evaluated for each peak, and the Debye–Scherrer equation was used to compute the average size of $TiO_2$ NPs, which was found to be 15.61 nm.

**3.2.3. UV-vis absorption spectroscopy.** The UV-Vis absorption spectrum of $TiO_2$ NPs is presented in Fig. 2C. The UV-Vis spectroscopy confirmed the formation of $TiO_2$ NPs since it exhibited 3 absorption peaks at 317.5 nm, 254.9 nm, and 204.8 nm. The collective oscillations of the $TiO_2$ NPs' surface electrons produced the Surface Plasmon Resonance (SPR), leading to the observed UV-Vis absorption. This is in line with previously reported studies of $TiO_2$ nanoparticles.[46,56]

**3.2.4. Structural analysis of $TiO_2$ NPs.** SEM was used to characterize the surface morphology of $TiO_2$ NPs. The SEM micrograph is presented in Fig. 3A and B, showing the $TiO_2$ NPs' uniform surface and porous nature. In addition, the NPs were shown to be agglomerated due to their tiny sizes, where similar results were previously reported.[59] On the other hand, the chemical composition of the prepared $TiO_2$ NPs by EDX

Table 2 EDX data of $TiO_2$ NPs

| Sample | Element | Weight% | Atomic% |
|---|---|---|---|
| $TiO_2$ NPs | Oxygen | 43.34 | 69.61 |
| | Titanium | 56.66 | 30.39 |
| | **Total** | **100.00** | **100.00** |

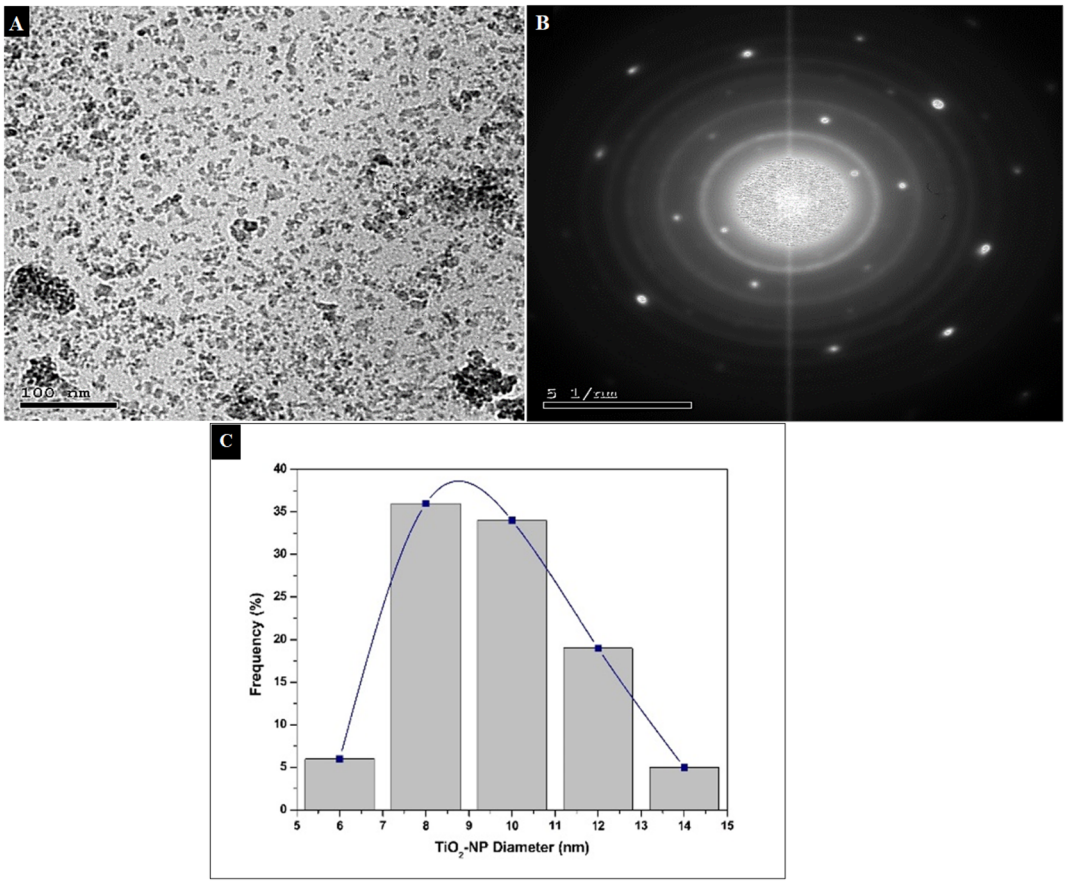


Fig. 4 (A) TEM micrograph of $TiO_2$ NPs, (B) SAED, and (C) diameter distribution histogram.

examination was characterized by measuring the energy of the X-rays emitted by the sample. The X-rays, characteristic of the nature of elements, can give accurate results for element detection.[60] The obtained EDX pattern of $TiO_2$ NPs (Fig. 3C) showed the presence of only Ti and O, which aligns with the EDX data presented in Table 2. The results confirm the high purity of the prepared $TiO_2$ NPs. These findings are in parallel with previously reported studies and confirmed the successful bioengineering of $TiO_2$ NPs.[59] Finally, EDX mapping was carried out to confirm the elements found in the EDX analysis as well as to find out their atomic distribution in the $TiO_2$ NPs. Our findings indicate a uniform distribution of the Ti and O solely with no other impurities, as presented in Fig. 3D. Thus, the SEM, EDX elemental analysis, and EDX mapping confirmed the successful preparation of pure $TiO_2$ NPs.[61]

**3.2.5. Morphological analysis of $TiO_2$ NPs.** TEM image for the prepared $TiO_2$ NPs is presented in Fig. 4A, showing the morphology of individual nanoparticles. The selected area electron diffraction (SAED) pattern (Fig. 4B) was investigated and showed sharp spots, confirming the NPs' crystalline structure. This confirmation is in agreement with the XRD results. The diameter of the $TiO_2$ NPs was measured using ImageJ (NIH, Bethesda, MD, USA), and the average diameter was found to be $8.69 \pm 1.93$ nm, ranging between 5.55 and 13.89 nm. This value is close to that obtained from the Debye–Scherrer equation. The nanoparticles' diameter distribution histogram is presented in Fig. 4C.[62] This optimized nano-size is crucial in improving the uptake of the NPs into the cancerous cells *via* passive targeting (EPR effect).[63]

### 3.3. Cell viability assay

To investigate the potency of our green $TiO_2$ NPs drug delivery system, a cell viability assay was conducted on the breast adenocarcinoma model (MCF), and the lung cancer cell line A-549. A normal non-tumorigenic cell line, MCF10A, served as a control to evaluate the apparent safety profile and selectivity index (SI). MCF-7 and A-549 are well-established models to study the effect of antitumor drugs on breast and

Table 3 Cellular viability of MCF-7, A-549, and normal MCF10A after exposure to $TiO_2$ NPs for 48 hours

| $IC_{50}$ on MCF-7 ($\mu g\ mL^{-1}$) | $CC_{50}$ on MCF10A | SI ($CC_{50}/IC_{50}$) |
|---|---|---|
| 1.73 | 15.17 | 8.77 |
| $IC_{50}$ on A549 ($\mu g\ mL^{-1}$) | $CC_{50}$ on MCF10A | SI ($CC_{50}/IC_{50}$) |
| 4.79 | 15.17 | 3.17 |

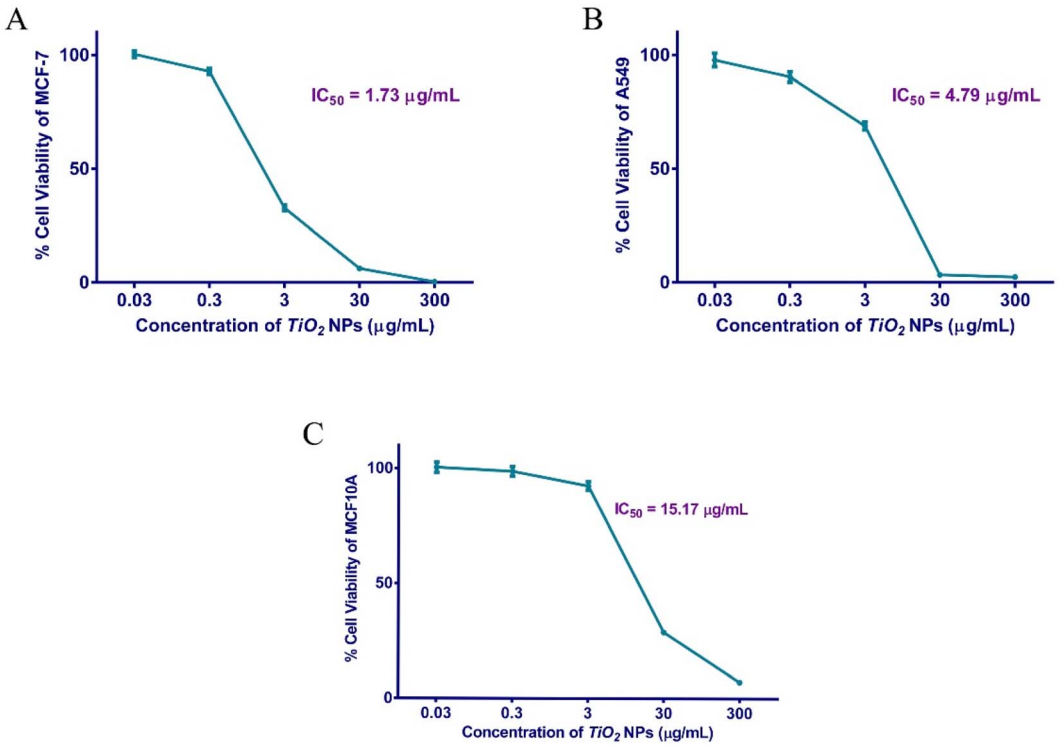


Fig. 5 Cellular viability of human MCF-7 (A), A-549 (B), and MCF10A (C) cells after exposure to different concentrations of $TiO_2$ NPs for 48 h.

lung cancer cells, respectively.[64–67] The half-maximal inhibitory concentration ($IC_{50}$) for $TiO_2$ NPs against MCF-7 was shown to be 1.73 μg $mL^{-1}$, whereas the $IC_{50}$ of $TiO_2$ NPs against the A-549 cell line was 4.79 μg $mL^{-1}$. The 50% cytotoxicity concentration of the NPs against the control cell line was 15.7 μg $mL^{-1}$.

The selectivity index (SI) for MCF-7 breast cancer cell lineage was a notable 8.77, indicating its pronounced therapeutic index, while SI for A-549 was a tolerable 3.17 (Table 3 and Fig. 5). A previous study was done on 4T1 breast BALB/c mouse tumor model using a different formulation of $TiO_2$ NPs, where the $IC_{50}$ was 4.11 μg $mL^{-1}$.[68] Sonochemically-synthesized $TiO_2$ NPs had an $IC_{50}$ of 60 μg $mL^{-1}$ on MCF-7.[69] A recent study conducted on a triple-negative breast cancer model using a different green $TiO_2$ NPs formulation (propolis-extract) showed a much higher $IC_{50}$ of 18.7 μg $mL^{-1}$.[70]

Similarly, our prepared $TiO_2$ NPs displayed strong anti-proliferative activity against the A-549 lung cancer model as compared to a previous study.[67] This cell viability assay indicates a potential candidate as a selective antineoplastic agent. Our data suggests the preferential uptake of the designed NPs by the leaky cancer cells, as compared to the normal control.[71] In addition, our findings proposed the safe potential use of $TiO_2$ NPs as a future alternative to the current chemotherapeutics that possess several systemic toxic effects.[72]

### 3.4. Apoptosis assay

Apoptosis is the regulated cell suicide that is activated upon incurred DNA damage, infection, stress, or aberrant cellular

Table 4 Apoptosis assay results of MCF-7 and A-549 cells after incubation with $TiO_2$ NPs for 48 h

| | Percent cell population[a] | | | |
|---|---|---|---|---|
| | MCF-7 cells | | A-549 cells | |
| Apoptotic stage | Control | $TiO_2$ treated | Control | $TiO_2$ treated |
| Necrosis cells (Q2-1) | 1.393 ± 0.2658 | **5.203 ± 0.7506 | 0.7267 ± 0.0208 | ***13.64 ± 0.9658 |
| Late apoptosis (Q2-2) | 1.76 ± 0.2685 | ***17.96 ± 1.517 | 1.070 ± 0.1153 | **2.133 ± 0.2937 |
| Viable cells (Q2-3) | 96.15 ± 0.168 | ***69.08 ± 2.801 | 98.13 ± 0.0907 | ***82.72 ± 1.227 |
| Early apoptosis (Q2-4) | 0.70 ± 0.1311 | ***7.76 ± 0.7758 | 0.07667 ± 0.0153 | **1.510 ± 0.3904 |

[a] The percent cell population is recorded as the average of triplicates ± SD. ** and *** indicatestatistical significance from the control where *P*-value ≤ 0.01 and ≤0.00, respectively.

process. It is a life-saving mechanism to prevent oncogenic transformation. Apoptosis is remarkably deregulated in cancer, displaying a hallmark of immortality and uncontrolled proliferation.[73,74] Cells undergoing apoptosis shrink, show cell membranes blebbing, DNA fragmented, cytoskeleton degraded, and phagocytosis signaled.[74,75] Tumor cells send various factors into the surrounding microenvironment to repress programmed cell death. In order to elucidate the molecular mechanism of our $TiO_2$ NPs-induced cell death, a standard apoptosis assay was conducted.

The gold-standard Annexin V/Propidium Iodide (AV/PI) assay was carried out to estimate the percentage of cells that have undergone programmed cell death (apoptosis) or inflammatory cell death (necrosis).[75,76] Living cells maintain an intact phospholipid membrane, internalizing phosphatidyl serine and preventing the entry of charged dyes into the cells. However, when cells die by apoptosis, the plasma membrane loses its integrity, displaying phosphatidyl serine facing outward.[75] Annexin V binds phosphatidyl serine and emits a signal that is detected by a Flow Cytometer. Propidium iodide intercalates the DNA of cells undergoing necrosis.[77]

MCF-7 cells treated for 48 h with $TiO_2$ NPs were compared to untreated cells. Our findings revealed that 17.96% of treated MCF-7 were in the late apoptotic phase, while 5.2% were in the necrotic stage. A-549 treated similarly showed 13.64% of the population in the necrosis stage (Table 4 and Fig. 6). The apoptotic and anticancer activities of $TiO_2$ NPs against cancer cells have been previously reported.[69,78] For instance, Wang *et al.* displayed a significant potential for $TiO_2$ NPs to stimulate apoptosis and produce DNA damage in A-549 cells.[78]

Apparently, the two cell lines responded differently after exposure to $TiO_2$ NPs for 48 hours. MCF-7 showed a significant programmed cell suicide, remarkably in late apoptosis, relative to necrotic cell death in A-549 cells. These results indicate the strong potential of greenly-synthesized $TiO_2$ NPs as candidate chemotherapeutic agents exerting an apoptotic effect in breast cancer.

### 3.5. Cell cycle assay

Actively dividing cells follow precise stages known as the cell cycle. In the first phase, G1, the cell grows and accumulates nutrients, organelles, and proteins needed for DNA replication. Meanwhile, the cells duplicate their chromosomes in the S and G2 phases and produce proteins needed for division, respectively. Finally, in the M stage, mitosis, the parent cell divides equally into two daughters. On the other hand,

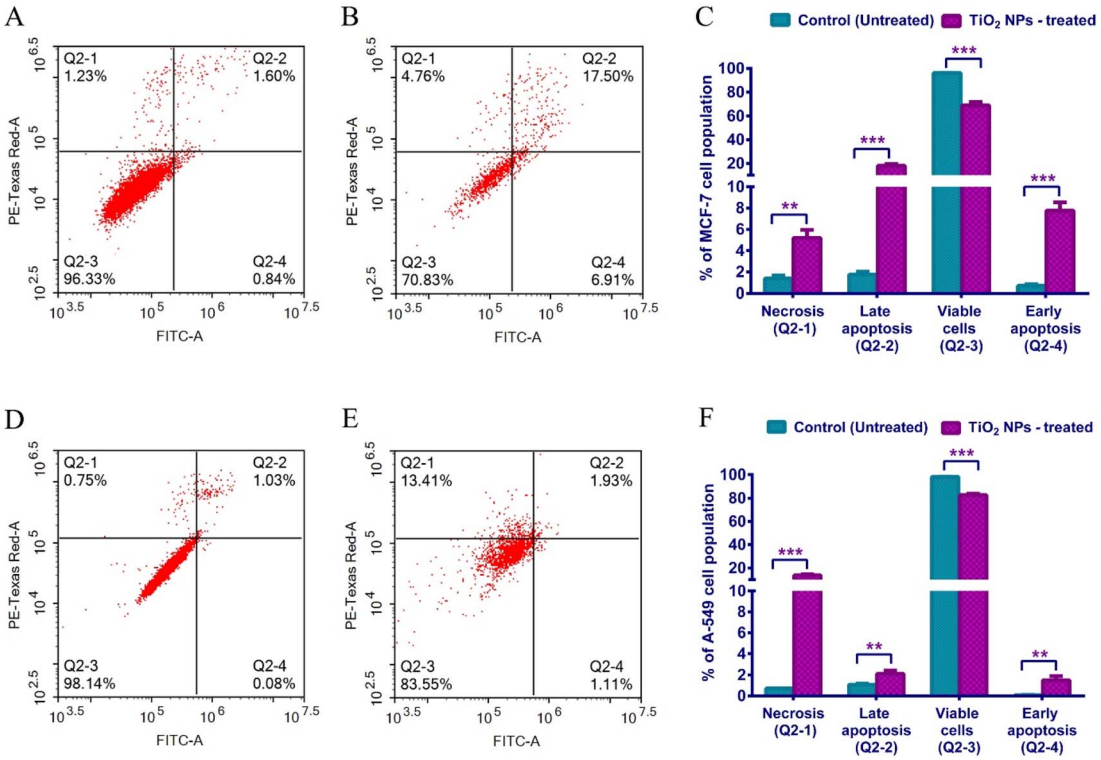


Fig. 6 Apoptosis assay in MCF-7 and A-549 following 48 h of incubation with $TiO_2$ NPs. (A) displays the untreated MCF-7 cells (Control), (B) shows the MCF-7 cells incubated with $TiO_2$ NPs for 48 h. (C) Graphical representation of the gold standard Annexin V/Propidium Iodide (AV/PI) assay on MCF-7 cells. (D) presents the untreated A-549 cells (control), (E) the A-549 cells after treatment with $TiO_2$ NPs for 48 h, and (F) Bar graph showing the apoptosis assay results on A-549 cells. The cytograms' quadrants are demonstrated as Q2-1 (necrotic cells, $AV^-/PI^+$), Q2-2 (late apoptotic cells, $AV^+/PI^+$), Q2-3 (normal cells, $AV^-/PI^-$), Q2-4 (early apoptotic cells, $AV^+/PI^-$). Data represented is the average of triplicate experimental trials ± SD. **refers to $p$-value ≤ 0.01 *vs.* control cells, ***refers to $p$-value ≤ 0.001 *vs.* control cells.

Table 5 Cell cycle assay of treated *vs.* untreated MCF-7 and A-549 cells using $TiO_2$ NPs

| Cell cycle phase | MCF-7 | | A-549 | |
|---|---|---|---|---|
| | Control (untreated) | $TiO_2$-treated | Control (untreated) | $TiO_2$-treated |
| Sub-G1 | 0.3233 ± 0.1557 | ***22.52 ± 3.455 | 0.7133 ± 0.1137 | ***82.30 ± 1.570 |
| G1 | 53.16 ± 2.061 | ***25.99 ± 0.49 | 74.17 ± 1.130 | ***4.837 ± 1.341 |
| S | 20.59 ± 1.202 | **10.98 ± 2.525 | 16.25 ± 0.8317 | **7.947 ± 0.8903 |
| G2 | 29.78 ± 1.768 | ***50.43 ± 1.595 | 8.317 ± 1.241 | *4.350 ± 1.599 |

* refers to $p$-value ≤ 0.05 *vs.* control cells, ** refers to $p$-value ≤ 0.01 *vs.* control cells and *** refers to $p$-value ≤ 0.001 *vs.* control cells.

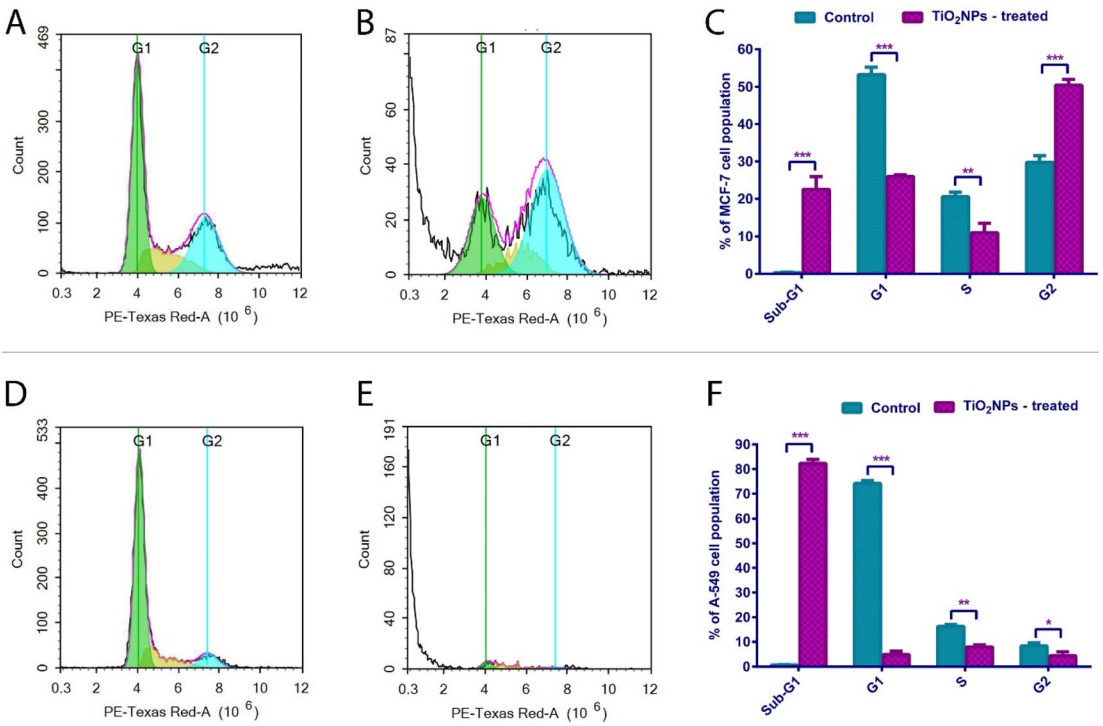


Fig. 7 (A) Untreated MCF-7 (control), (B) MCF-7 exposed to $TiO_2$ NPs for 48 h, (C) Bar graph showing the cellular distribution at each phase of the MCF-7 cell cycle, (D) Untreated A-549 (control), (E) A-549 cells exposed to $TiO_2$ NPs for 48 h, (F) A-549 cell cycle analysis graph. Data represented is the average of triplicate experimental trials ± SD. **refers to $p$-value ≤ 0.01 *vs.* control cells and ***refers to $p$-value ≤ 0.001 *vs.* control cells.

undividing cells or those lacking the necessary nutrient/growth factors for DNA replication enter a quiescent phase. For the cell to proceed from one stage into the following, specialized proteins (cyclins and cyclin-dependent kinases) come into play. Moreover, checkpoints occur to validate the process and make sure no errors occur. G1/S and G2/M are hallmark checkpoints regulating the cell transition through the cell cycle phases. Checkpoints are precisely orchestrated by cyclins, kinases and modulator (activator/inhibitor) proteins.[79] A cell cycle assay is based on quantifying DNA concentrations and visualizing chromatin patterns in different cell cycle stages. This is detected using a flow cytometer.[79–81]

A standard cell cycle assay was conducted according to the established guidelines[82,83] to interpret the cell death mechanisms of MCF-7 and A-549 cells exposed to $TiO_2$ NPs for 48 hours relative to the untreated controls.

Interestingly, 22.52% of $TiO_2$ NPs treated MCF-7 cells were arrested in the Sub-G1 phase. A remarkable 50.43% of $TiO_2$ NPs treated MCF-7 cells were arrested in the G2 phase of the cell cycle before proceeding to mitotic division (Table 5 and Fig. 7). This showed a marked reduction of cellular population in G1 relative to the reference cells. Less than 11% of the cellular population was in the S phase. This aligns with our findings that a significant proportion of MCF-7 cells undergo late apoptosis. Taken together, MCF-7 cells treated with $TiO_2$ NPs show a hallmark apoptotic profile early enough in the cell cycle. It represents a dynamic cell cycle arrest model at multiple phases, insinuating interplay with modulators of alternative

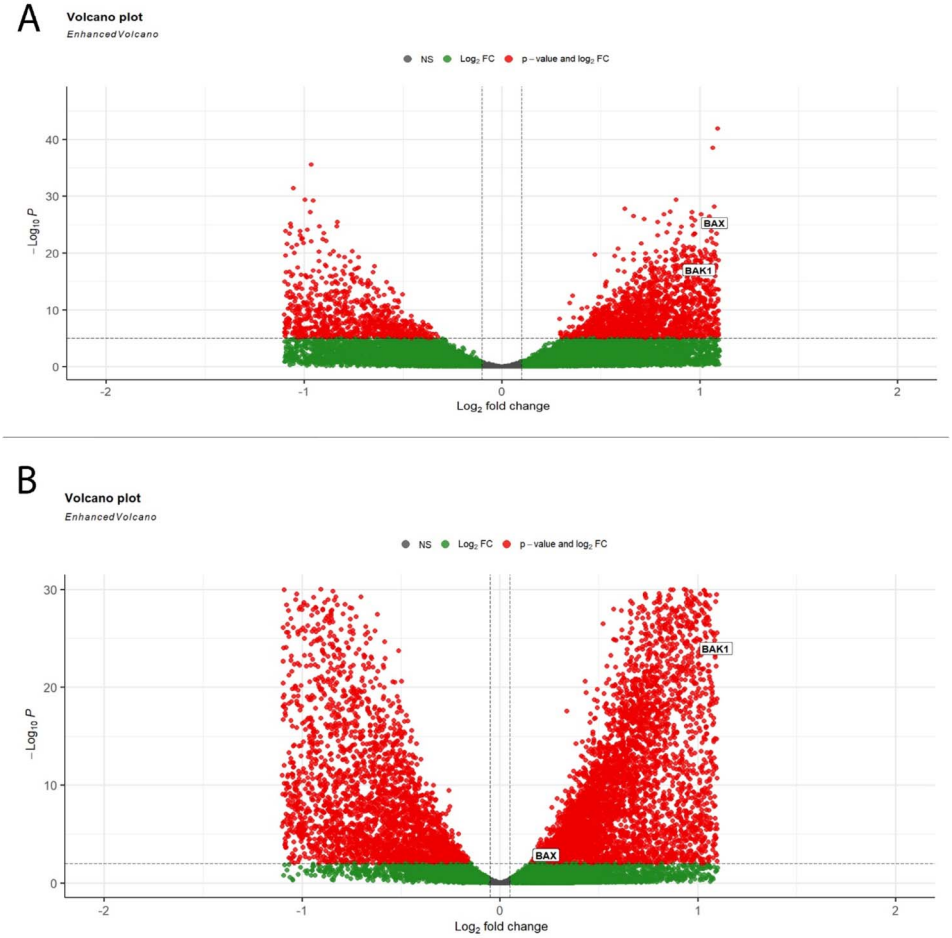


Fig. 8 Volcano plots of DEGs; (A) representative Volcano plot of DEGs from TCGA-BRCA (breast cancer) with thresholds of a $P$ value < 0.05 and $|\log_2$ fold change$|$ > 0.1, (B) representative Volcano plot of DEGs from TCGA-LUSC (lung cancer) with thresholds of a $P$ value < 0.05 and $|\log_2$ fold change$|$ > 0.1.

checkpoints. This is particularly significant in tumors escaping one checkpoint and evading cell cycle arrest. Anticancer drugs targeting the G2 phase offer a plausible choice if tumor cells evade the G1/S checkpoint.[84]

On the other hand, 82.3% of A-549 treated cells were shown to be in the Sub-G1 phase, denoting an extensive DNA fragmentation/loss event and a pronounced ability to cease cell cycle progression before the G1/S checkpoint.[85] Our findings suggest complementary evidence of the pronounced cytotoxicity of the synthesized $TiO_2$ NPs. Our findings aligned very well with a previous study which reported a highly remarkable elevation in the frequency of several mammalian cells in the sub-G1 phase of the cell cycle following exposure to $TiO_2$ NPs.[86]

### 3.6. Bioinformatic analysis to select top targeted genes for RT-qPCR analysis

Our bioinformatics workflow was primarily concerned with identifying differentially expressed genes that showed differences in expression in tumor samples comparable to normal solid samples in both TCGA-BRCA and TCGA-LUSC. This difference was assessed in terms of both fold-change (FC) and statistical significance adjusted $p$-value. In both datasets, the volcanic plot illustrated that Bax and Bak1 genes were upregulated and differentially expressed in tumor samples compared to normal samples, as shown in Fig. 8. Based on the obtained results, Bax and Bak1 genes were selected for further gene expression analysis using RT-qPCR.

### 3.7. Gene expression for apoptotic markers

Apoptosis could be induced by either intrinsic or extrinsic pathways. The intrinsic pathway, also known as mitochondrial-mediated cell death, is activated upon the reception of an apoptotic stimulus. This is subsequently followed by activating a series of proteins, eventually leading to the oligomerization of the cytosolic Bax and Bak proteins. Then, these apoptotic proteins insert themselves into the outer mitochondrial membrane, leading to pore-formation and increased

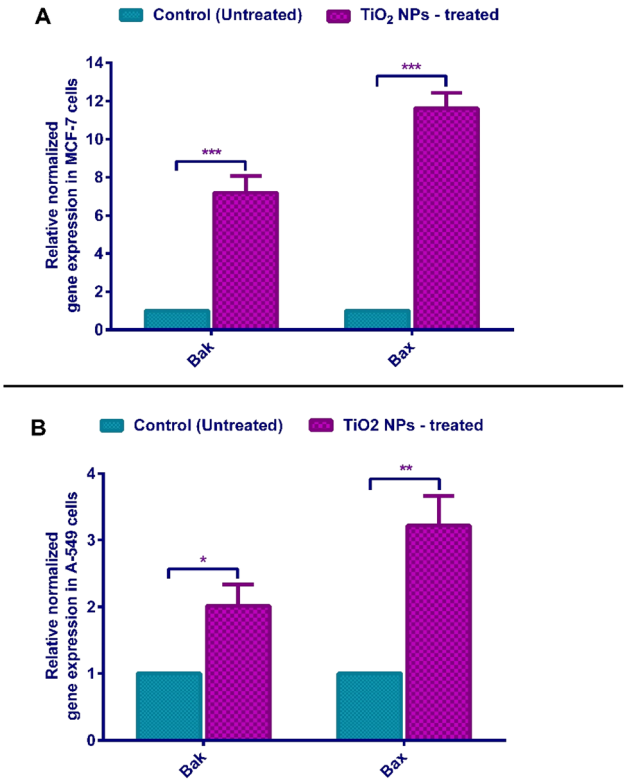


Fig. 9 (A) Relative normalized gene expression in MCF-7 cells, (B) relative normalized gene expression in A-549 cells using qPCR. Data represented is the average of triplicate experimental trials ± SD. **refers to $p$-value ≤ 0.01 *vs.* control cells, ***refers to $p$-value ≤ 0.001 *vs.* control cells.

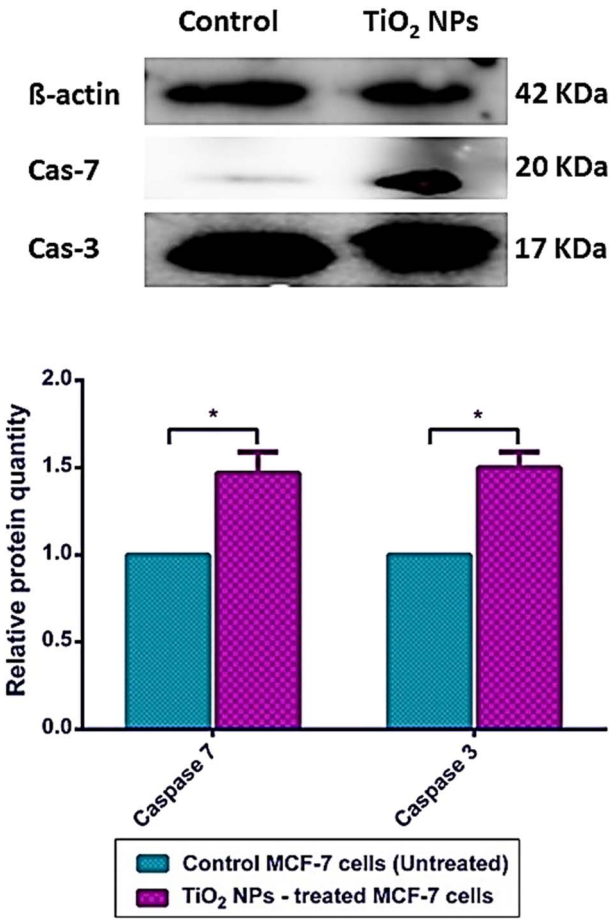


Fig. 10 Relative protein expression of caspase 3 and caspase 7 in treated and untreated MCF-7 cells, β-actin, was used as the internal reference standard. Data represented is the average of triplicate experimental trials ± SD. The band intensity was obtained using the ChemiDoc imaging system Biorad.

mitochondrial permeability. Afterwards, cytochrome C, is released from the mitochondria into the cytoplasm, activating an apoptosome and caspase 9.[87] These mediators eventually activate effector caspases 3 and 7, leading to DNA degradation, cell membrane blebs, cytoskeleton destruction, cell shrinkage, and phagocytosis by immune cells. Cancer cells cannot usually undergo programmed-cell suicide and thus replicate indefinitely.[76]

Quantitative PCR (qPCR) was carried out to assess the relative normalized gene expression of two apoptosis hallmark genes, namely, "Bcl-2 associated X protein" (Bax) and "Bcl-2 antagonist/killer" (Bak). β-Actin was used as the internal reference (housekeeping gene).[88] Upon treatment with $TiO_2$ NPs, MCF-7 cells show a 7.17-fold change in BakAK and 11.62-fold in Bax expression (Fig. 9). Treated A-549 cells witnessed a 2.01 and 3.21 folds increase for Bak and Bax, respectively (Fig. 9). These findings complement our apoptosis and cell cycle results, which indicate that $TiO_2$ NPs induce programmed cell suicide through the Bax/Bak-mediated outer membrane permeabilization (MOMP),[75,83,89] which successively leads to caspase-dependent apoptosis. Interestingly, Bak and Bax proteins were recently shown to orchestrate necrotic death[87] observed in A-549 cells.[90–92] Hence, our greenly synthesized $TiO_2$ NPs are strong candidate antitumor agents causing neat cell death (*via* intrinsic apoptotic pathway).

### 3.8. Immunoblotting for apoptotic proteins

To further confirm the mechanism of action of our greenly synthesized $TiO_2$ NPs as a potential pro-apoptotic agent, the protein expression of caspases 3 and 7 was quantifiably analyzed by western blot, and the quantification was done utilizing the ChemiDoc imaging system. Our findings showed that caspases 3 and 7 are significantly overexpressed (about 1.5 increase) in $TiO_2$ NPs treated MCF-7 relative to untreated cells (Fig. 10). Likewise, $TiO_2$ NPs were noticed to significantly elevate the expression of caspase-3 in the hepatoma cell line (HepG2), as well as the activity of caspase 3/7.[93] In another study, the $TiO_2$ NPs synthesized with the aid of *Lactobacillus* bacteria have also caused a significant upregulation of caspase 3 in human colorectal cancer cells (HT-29) and actuation of the intrinsic apoptosis pathway.[94] A previous study on human

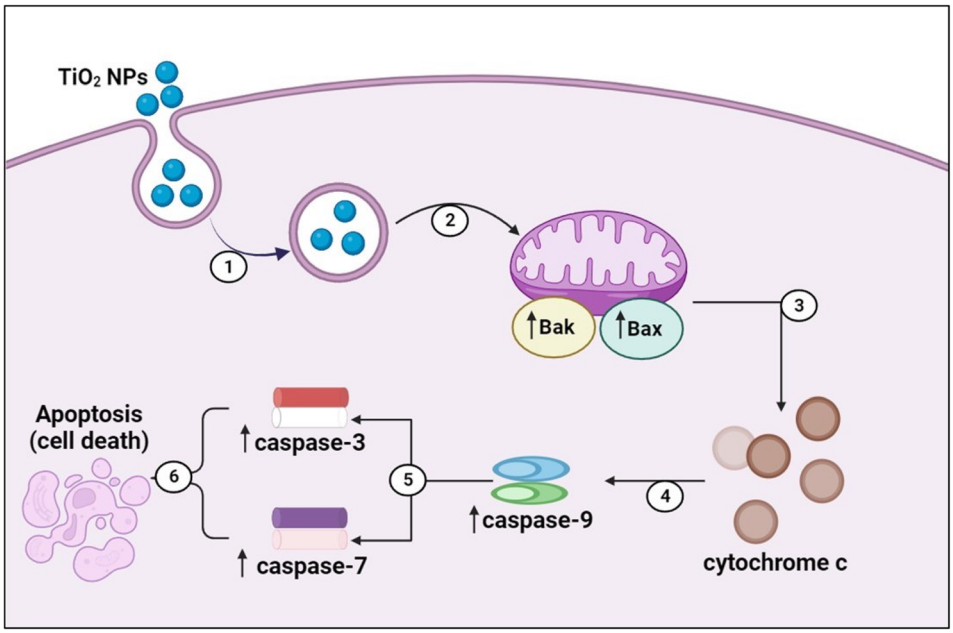


Fig. 11 The mechanism by which $TiO_2$ NPs induce mitochondrial-mediated apoptosis of cancer cells. (1) Endosomal uptake of $TiO_2$ NPs, (2) mitochondrial outer membrane perturbation, (3) cytochrome C release into the cytosol, (4) activation of initiator caspase 9, (5) activation of executioners caspases (3 and 7), and (6) induction of apoptosis.

hepatocarcinoma cells (SMMC-7721) revealed potentiated effects for $TiO_2$ NPs when combined with doxorubicin (DOX) in increasing the caspase-3 protein compared to sole DOX treatment.[95]

Meanwhile, treatment of SMMC-7721 hepatocarcinoma with $TiO_2$ NPs alone showed a slight, not yet significant, increase in caspase 3 protein expression.[95] Our findings agree with the results of the apoptosis and cell cycle assays above, which showed that $TiO_2$ NPs induce mitochondrial-mediated apoptotic cytolysis.

Caspases are critical proteins for regulating programmed cell death and inflammatory reactions. Thus, inadequate caspase activation can endorse carcinogenesis. In this regards, caspases have been generally classified by their established functions in programmed cell death into caspase-3, -6, -7, -8, and -9, which are sub-categorized according to their mode of action into initiator caspases (caspase-8 and -9) and killer caspases (caspase-3, -6, and -7).[96] $TiO_2$ NPs are proposed to exert their anticancer activities *via* mitochondrion-based cell death (Fig. 11). In this context, $TiO_2$ NPs are internalized into cancer cells *via* endosomal uptake. Then, intracellularly, the $TiO_2$ NPs significantly increased the gene expression of Bak and Bax apoptotic markers and their relative proteins. This stimulates the intrinsic apoptotic pathway where Bak and Bax are translocated into the mitochondrion of the cancer cell, increasing the permeability of its outer membrane and thus releasing cytochrome C pro-apoptotic protein from the mitochondrial matrix into the cytosol.[91,92,96] The mitochondrial perturbation and cytochrome C release activate the initiator caspase 9. Once activated, caspase 9 activates the executioners of apoptosis (caspases 3 and 7) *via* internal cleavage of large and small subunits. The effector caspases 3 and 7 induce apoptosis *via* protein crosslinking, DNA fragmentation, and hydrolysis of nuclear proteins.[96]

### 3.9. Molecular docking of $TiO_2$ NPs in the active sites of caspase-3 and EGFR-TK

$TiO_2$ NPs could bind to both crystal structure pockets with binding affinities of −4.16 and −4.06 kcal $mol^{-1}$ for PDB IDs 2XYG and 1M17, respectively. Fig. 12A shows the $TiO_2$ NPs bound to caspase-3 active pocket (shown in green sticks), including 7 main residues: Arg 64, Ser 120, His 121, Gly 122, Gln 161, Ala 162 and Cys 163. The NP's two oxygen atoms formed 4 H-bonds; 2 of them were with Gly 122, one with Ser 120, and the last with His 121.

EGFR-TK is widely overexpressed in breast and lung cancers, where it contributes to the tumorigenesis process by promoting cellular growth, angiogenesis, metastasis, and resistance to chemotherapy.[97] In this context, a growing body of evidence has emerged over the past 20 years regarding the targeted inhibition of the EGFR-TK family as a cancer treatment approach.[97] The current study demonstrated several binding interactions for $TiO_2$ NPs, where it was able to form 2 H-bonds with Gln-767, 2 H-bonds with Arg 752, and an H-bond with Val 750 in the active site of EGFR-TK, Fig. 12B. Therefore, $TiO_2$ NPs is suggested to interfere with EGFR-TK and reduce cellular proliferation by limiting the activity of EGFR-TK in the tumor model. The study

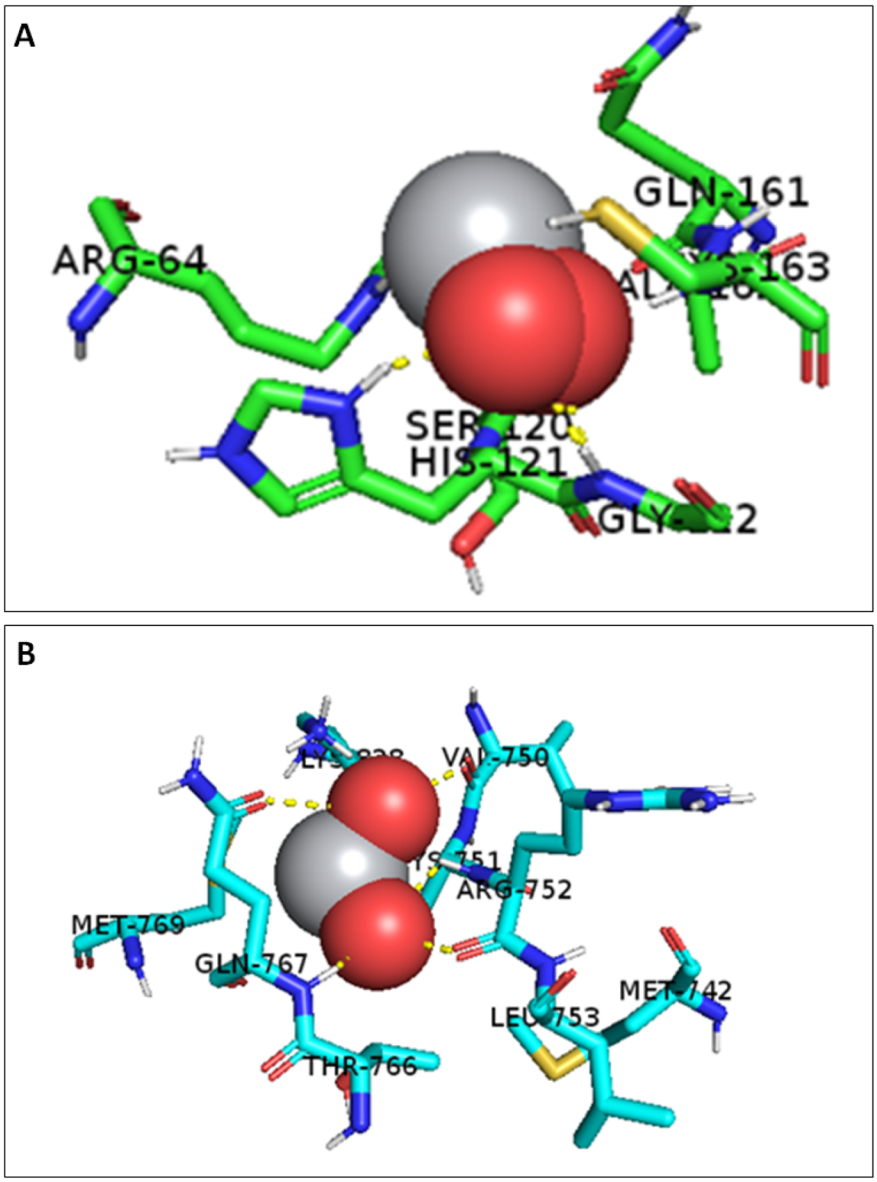


Fig. 12 (A) 3D interactions of $TiO_2$ NPs with caspase 3 active pocket (PDB ID: 2XYG) and (B) 3D interactions of $TiO_2$ NPs with EGFR-TK active pocket (PDB ID: 1M17). The active site residues are shown in blue sticks.

suggests further preclinical investigations for using $TiO_2$ NPs as an EGFR-TK inhibitor.

## 4. Conclusion

There is a dire need to discover novel chemotherapeutic agents or enhance the efficacy of existing ones. To this end, we bio-synthesized $TiO_2$ NPs using an eco-friendly novel sonochemical approach and tested its effect on two cancer cell lines. We used *Ocimum basilicum* essential oil as a natural reductant and capping agent to efficiently biosynthesize $TiO_2$ NPs with outstanding surface properties and biochemical profiles. Our $TiO_2$ NPs exhibited potent cytotoxic effects on breast (MCF-7) and lung cancer (A-549) cell populations while maintaining an excellent selectivity index on normal cells. Apoptosis and cell cycle assays indicated that $TiO_2$ NPs induced apoptosis and arrested the cell cycle in the subG1 phase in both tumor models. Gene expression analysis confirmed the up-regulation of BAX and BAK genes, emphasizing the intrinsic mitochondrial apoptosis mechanism. Protein expression analysis of caspases 3 and 7 enzymes showed a remarkable over-expression relative to the control untreated cells. The molecular docking study also demonstrated good binding potential for $TiO_2$ NPs with two of the common targets in breast and lung cancers (caspase 3 and EGFR-TK). In a nutshell, we herein report the green synthesis of $TiO_2$ NPs with potent cytotoxicity and high selectivity profiles capable of inducing apoptosis in both breast and lung cancer cells *via* the mitochondrial-mediated permeability approach.

Moreover, the $TiO_2$ NPs exhibited several binding interactions with EGFR-TK, reinforcing their ability to induce apoptosis and inhibit cellular growth.

## Data availability

Data is contained within the article and ESI.†

## Conflicts of interest

The authors declare no conflict of interest.

## Acknowledgements

This work was funded by RSC Research Fund grant (ID: R22-3870733873) from the Royal Society of Chemistry to Dr Sherif Ashraf Fahmy. The authors are thankful to the Deanship of Scientific Research at King Khalid University for funding this work through general research project with project grant number GRP/111/44. Also, the authors thank Nanogate-Egypt Company for conducting the Transmission Electron Microscopy (TEM) analysis and taking the TEM images for the samples in the company's facility.

## References

1 NCI, *Cancer Statistics*, 2023, **https://www.cancer.gov/about-cancer/understanding/statistics**.
2 WHO, *W.H.O. Cancer*, 2023, **https://www.who.int/health-topics/cancer#tab=tab_1**.
3 D. Hanahan and R. A. Weinberg, Hallmarks of cancer: the next generation, *Cell*, 2011, **144**(5), 646–674.
4 F. Bray, *et al.*, Global cancer statistics 2018: GLOBOCAN estimates of incidence and mortality worldwide for 36 cancers in 185 countries, *Ca-Cancer J. Clin.*, 2018, **68**(6), 394–424.
5 T. A. Moo, *et al.*, Overview of Breast Cancer Therapy, *PET Clin.*, 2018, **13**(3), 339–354.
6 B. Mansoori, *et al.*, The Different Mechanisms of Cancer Drug Resistance: A Brief Review, *Adv. Pharm. Bull.*, 2017, **7**(3), 339–348.
7 I. Ritacco, *et al.*, Hydrolysis in acidic environment and degradation of satraplatin: a joint experimental and theoretical investigation, *Inorg. Chem.*, 2017, **56**(10), 6013–6026.
8 G. Mattheolabakis and C. M. Mikelis, Nanoparticle Delivery and Tumor Vascular Normalization: The Chicken or The Egg?, *Front. Oncol.*, 2019, **9**, 1227.
9 A. H. AbuBakr, H. A. Hassan, A. Abdalla, O. M. Khowessah and G. A. Abdelbary, Therapeutic potential of cationic bilosomes in the treatment of carrageenan-induced rat arthritis *via* fluticasone propionate gel, *Int. J. Pharm.*, 2023, **635**, 122776.
10 S. A. Fahmy, *et al.*, Ozonated Olive Oil: Enhanced Cutaneous Delivery *via* Niosomal Nanovesicles for Melanoma Treatment, *Antioxidants*, 2022, **11**(7), 1318.
11 R. A. Youness, *et al.*, Oral Delivery of Psoralidin by Mucoadhesive Surface-Modified Bilosomes Showed Boosted Apoptotic and Necrotic Effects against Breast and Lung Cancer Cells, *Polymers*, 2023, **15**(6), 1464.
12 S. A. Fahmy, *et al.*, Molecular Engines, Therapeutic Targets, and Challenges in Pediatric Brain Tumors: A Special Emphasis on Hydrogen Sulfide and RNA-Based Nano-Delivery, *Cancers*, 2022, **14**(21), 5244, DOI: **10.3390/cancers14215244**.
13 N. K. Sedky, *et al.*, Box–Behnken design of thermo-responsive nano-liposomes loaded with a platinum (IV) anticancer complex: evaluation of cytotoxicity and apoptotic pathways in triple negative breast cancer cells, *Nanoscale Adv.*, 2023, **5**, 5399–5413.
14 N. K. Sedky, *et al.*, Co-Delivery of Ylang Ylang Oil of Cananga odorata and Oxaliplatin Using Intelligent pH-Sensitive Lipid-Based Nanovesicles for the Effective Treatment of Triple-Negative Breast Cancer, *Int. J. Mol. Sci.*, 2023, **24**(9), 8392.
15 R. Khursheed, *et al.*, Biomedical applications of metallic nanoparticles in cancer: Current status and future perspectives, *Biomed. Pharmacother.*, 2022, **150**, 112951.
16 A. R. Al Jayoush, H. A. Hassan, H. Asiri, M. Jafar, R. Saeed, R. Harati and M. Haider, Niosomes for nose-to-brain delivery: a non-invasive versatile carrier system for drug delivery in neurodegenerative diseases, *J. Drug Delivery Sci. Technol.*, 2023, 105007.
17 S. G. Abonashey, H. A. Hassan, M. A. Shalaby, A. G. Fouad, E. Mobarez and H. A. El-Banna, Formulation, pharmacokinetics, and antibacterial activity of florfenicol-loaded niosome, *Drug Delivery Transl. Res.*, 2023, 1–16.
18 M. H. Alyami, *et al.*, Retama monosperma chemical profile, green synthesis of silver nanoparticles, and antimicrobial potential: a study supported by network pharmacology and molecular docking, *RSC Adv.*, 2023, **13**(37), 26213–26228.
19 P. S. Jassal, *et al.*, Green synthesis of titanium dioxide nanoparticles: Development and applications, *J. Agric. Food Res.*, 2022, 100361.
20 C. Zarzzeka, *et al.*, Use of titanium dioxide nanoparticles for cancer treatment: A comprehensive review and bibliometric analysis, *Biocatal. Agric. Biotechnol.*, 2023, 102710.
21 H. Iqbal, *et al.*, Breast cancer inhibition by biosynthesized titanium dioxide nanoparticles is comparable to free doxorubicin but appeared safer in BALB/c mice, *Materials*, 2021, **14**(12), 3155.
22 R. Mund, *et al.*, Novel titanium oxide nanoparticles for effective delivery of paclitaxel to human breast cancer cells, *J. Nanopart. Res.*, 2014, **16**, 1–12.
23 S. Sharmin, *et al.*, Nanoparticles as antimicrobial and antiviral agents: A literature-based perspective study, *Heliyon*, 2021, **7**(3), e06456.
24 S. A. Fahmy, *et al.*, Green synthesis of platinum and palladium nanoparticles using Peganum harmala L. seed alkaloids: Biological and computational studies, *Nanomaterials*, 2021, **11**(4), 965.

25 S. Ying, *et al.*, Green synthesis of nanoparticles: Current developments and limitations, *Environ. Technol. Innovation*, 2022, **26**, 102336.
26 M. Aravind, M. Amalanathan and M. S. M. Mary, Synthesis of $TiO_2$ nanoparticles by chemical and green synthesis methods and their multifaceted properties, *SN Appl. Sci.*, 2021, **3**, 1–10.
27 M. Altikatoglu, *et al.*, Green synthesis of copper oxide nanoparticles using Ocimum basilicum extract and their antibacterial activity, *Fresenius Environ. Bull.*, 2017, **25**(12), 7832–7837.
28 B. Thakur, A. Kumar and D. Kumar, Green synthesis of titanium dioxide nanoparticles using Azadirachta indica leaf extract and evaluation of their antibacterial activity, *S. Afr. J. Bot.*, 2019, **124**, 223–227.
29 N. M. Aboeita, *et al.*, Enhanced anticancer activity of nedaplatin loaded onto copper nanoparticles synthesized using red algae, *Pharmaceutics*, 2022, **14**(2), 418.
30 H. A. Salam and R. Sivaraj, Ocimum basilicum L. var. purpurascens Benth.-LAMIACEAE Mediated Green Synthesis and Characterization of Titanium Dioxide Nanoparticles, *Adv. Bio Res.*, 2014, **5**(3), 10–16.
31 A. R. Malik, *et al.*, Green synthesis of RGO-ZnO mediated Ocimum basilicum leaves extract nanocomposite for antioxidant, antibacterial, antidiabetic and photocatalytic activity, *J. Saudi Chem. Soc.*, 2022, **26**(2), 101438.
32 A. S. Abdelsattar, *et al.*, Utilization of Ocimum basilicum extracts for zinc oxide nanoparticles synthesis and their antibacterial activity after a novel combination with phage, *Mater. Lett.*, 2022, **309**, 131344.
33 K. Arshad Qamar, *et al.*, Anticancer activity of Ocimum basilicum and the effect of ursolic acid on the cytoskeleton of MCF-7 human breast cancer cells, *Lett. Drug Des. Discovery*, 2010, **7**(10), 726–736.
34 W. Tan, *et al.*, Surface coating changes the physiological and biochemical impacts of nano-TiO2 in basil (Ocimum basilicum) plants, *Environ. Pollut.*, 2017, **222**, 64–72.
35 N. Lagopati, *et al.*, Nanomedicine: Photo-activated nanostructured titanium dioxide, as a promising anticancer agent, *Pharmacol. Ther.*, 2021, **222**, 107795.
36 X. Zhu, K. Pathakoti and H.-M. Hwang, Green synthesis of titanium dioxide and zinc oxide nanoparticles and their usage for antimicrobial applications and environmental remediation, in *Green Synthesis, Characterization and Applications of Nanoparticles*, Elsevier, 2019, pp. 223–263.
37 S. A. Fahmy, *et al.*, Green extraction of essential oils from Pistacia lentiscus resins: encapsulation into Niosomes showed improved preferential cytotoxic and apoptotic effects against breast and ovarian cancer cells, *J. Drug Delivery Sci. Technol.*, 2023, **87**, 104820.
38 N. K. Mahdy, *et al.*, Toward Scaling up the Production of Metal Oxide Nanoparticles for Application on Washable Antimicrobial Cotton Fabrics, *ACS Omega*, 2022, **7**(43), 38942–38956.
39 S. Kamiloglu, *et al.*, Guidelines for cell viability assays, *Food Front.*, 2020, **1**(3), 332–349.
40 T. D. Schmittgen and K. J. Livak, Analyzing real-time PCR data by the comparative CT method, *Nat. Protoc.*, 2008, **3**(6), 1101–1108.
41 C. E. Bohl, *et al.*, Structural basis for accommodation of nonsteroidal ligands in the androgen receptor, *J. Biol. Chem.*, 2005, **280**(45), 37747–37754.
42 P. Wee and Z. Wang, Epidermal growth factor receptor cell proliferation signaling pathways, *Cancers*, 2017, **9**(5), 52.
43 M. Westwood, *et al.*, Epidermal growth factor receptor tyrosine kinase (EGFR-TK) mutation testing in adults with locally advanced or metastatic non-small cell lung cancer: a systematic review and cost-effectiveness analysis, *Health Technol. Assess.*, 2014, **18**(32), 1.
44 S. Chibber and I. Ahmad, Molecular docking, a tool to determine interaction of CuO and $TiO_2$ nanoparticles with human serum albumin, *Biochem. Biophys. Rep.*, 2016, **6**, 63–67.
45 L. Jin, *et al.*, Breast cancer lung metastasis: Molecular biology and therapeutic implications, *Cancer Biol. Ther.*, 2018, **19**(10), 858–868.
46 M. Z. Ahmad, *et al.*, Green synthesis of titanium dioxide nanoparticles using ocimum sanctum leaf extract: *in vitro* characterization and its healing efficacy in diabetic wounds, *Molecules*, 2022, **27**(22), 7712.
47 V. Malapermal, *et al.*, Enhancing antidiabetic and antimicrobial performance of Ocimum basilicum, and *Ocimum sanctum* (L.) using silver nanoparticles, *Saudi J. Biol. Sci.*, 2017, **24**(6), 1294–1305.
48 P. R. More, *et al.*, Antimicrobial applications of green synthesized bimetallic nanoparticles from Ocimum basilicum, *Pharmaceutics*, 2022, **14**(11), 2457.
49 D. P. Bezerra, *et al.*, The dual antioxidant/prooxidant effect of eugenol and its action in cancer development and treatment, *Nutrients*, 2017, **9**(12), 1367.
50 É. R. Q. Dos Santos, *et al.*, Linalool as a therapeutic and medicinal tool in depression treatment: a review, *Curr. Neuropharmacol.*, 2022, **20**(6), 1073.
51 A. F. Ahmed, *et al.*, Antioxidant activity and total phenolic content of essential oils and extracts of sweet basil (*Ocimum basilicum* L.) plants, *Food Sci. Hum. Wellness*, 2019, **8**(3), 299–305.
52 T. Aburjai, *et al.*, Chemical Compositions and Anticancer Potential of Essential Oil from Greenhouse-cultivated Ocimum basilicum Leaves, *Indian J. Pharm. Sci.*, 2020, **82**(1), 178–183.
53 O. V. Kharissova, *et al.*, Greener synthesis of chemical compounds and materials, *R. Soc. Open Sci.*, 2019, **6**(11), 191378.
54 J. O. Tijani, M. M. Ndamitso and A. S. Abdulkareem, Facile synthesis and characterization of $TiO_2$ nanoparticles: X-ray peak profile analysis using Williamson–Hall and Debye–Scherrer methods, *Int. Nano Lett.*, 2021, **11**, 241–261.
55 N. Horti, *et al.*, Synthesis and photoluminescence properties of titanium oxide ($TiO_2$) nanoparticles: Effect of calcination temperature, *Optik*, 2019, **194**, 163070.
56 R. Aswini, S. Murugesan and K. Kannan, Bio-engineered $TiO_2$ nanoparticles using Ledebouria revoluta extract:

Larvicidal, histopathological, antibacterial and anticancer activity, *Int. J. Environ. Anal. Chem.*, 2021, **101**(15), 2926–2936.

57 W. Ahmad, K. K. Jaiswal and S. Soni, Green synthesis of titanium dioxide ($TiO_2$) nanoparticles by using Mentha arvensis leaves extract and its antimicrobial properties, *Inorg. Nano-Met. Chem.*, 2020, **50**(10), 1032–1038.

58 T. Luttrell, *et al.*, Why is anatase a better photocatalyst than rutile?-Model studies on epitaxial $TiO_2$ films, *Sci. Rep.*, 2014, **4**(1), 4043.

59 O. Alameer, *et al.*, Expoloriting of graphene oxide for improving physical properties of $TiO_2$ (NPs): toward photovoltaic devices and wastewater remediation approaches, *Eur. Phys. J. Plus*, 2022, **137**(10), 1160.

60 N. Raval, *et al.*, Importance of physicochemical characterization of nanoparticles in pharmaceutical product development, *Basic Fundam. Drug Delivery*, 2019, 369–400.

61 U. Baig, *et al.*, Single step production of high-purity copper oxide-titanium dioxide nanocomposites and their effective antibacterial and anti-biofilm activity against drug-resistant bacteria, *Mater. Sci. Eng., C*, 2020, **113**, 110992.

62 M. A. E. A. A. A. El-Remaily, A. M. Abu-Dief and O. Elhady, Green synthesis of $TiO_2$ nanoparticles as an efficient heterogeneous catalyst with high reusability for synthesis of 1,2-dihydroquinoline derivatives, *Appl. Organomet. Chem.*, 2019, **33**(8), e5005.

63 S. A. Fahmy, *et al.*, Thermosensitive Liposomes Encapsulating Nedaplatin and Picoplatin Demonstrate Enhanced Cytotoxicity against Breast Cancer Cells, *ACS Omega*, 2022, **7**(46), 42115–42125.

64 H.-r. Moon, *et al.*, Subtype-specific characterization of breast cancer invasion using a microfluidic tumor platform, *PLoS One*, 2020, **15**(6), e0234012.

65 L. Ziko, *et al.*, Antibacterial and anticancer activities of orphan biosynthetic gene clusters from Atlantis II Red Sea brine pool, *Microb. Cell Factories*, 2019, **18**(1), 1–16.

66 K. Nohara, F. Wang and S. Spiegel, Glycosphingolipid composition of MDA-MB-231 and MCF-7 human breast cancer cell lines, *Breast Cancer Res. Treat.*, 1998, **48**, 149–157.

67 L. Armand, *et al.*, Long-term exposure of A549 cells to titanium dioxide nanoparticles induces DNA damage and sensitizes cells towards genotoxic agents, *Nanotoxicology*, 2016, **10**(7), 913–923.

68 S. Abdel-Ghany, *et al.*, Vorinostat-loaded titanium oxide nanoparticles (anatase) induce G2/M cell cycle arrest in breast cancer cells *via* PALB2 upregulation, *3 Biotech*, 2020, **10**(9), 407.

69 K. Murugan, *et al.*, Hydrothermal synthesis of titanium dioxide nanoparticles: mosquitocidal potential and anticancer activity on human breast cancer cells (MCF-7), *Parasitol. Res.*, 2016, **115**(3), 1085–1096.

70 M. T. Hamed, *et al.*, Novel synthesis of titanium oxide nanoparticles: Biological activity and acute toxicity study, *Bioinorg. Chem. Appl.*, 2021, **2021**, 8171786.

71 S. A. Fahmy, *et al.*, Synthesis, characterization and host-guest complexation of asplatin: improved *in vitro* cytotoxicity and biocompatibility as compared to cisplatin, *Pharmaceuticals*, 2022, **15**(2), 259.

72 I. Ritacco, *et al.*, Hydrolysis in acidic environment and degradation of satraplatin: a joint experimental and theoretical investigation, *Inorg. Chem.*, 2017, **56**(10), 6013–6026.

73 A. R. Safa, Drug and apoptosis resistance in cancer stem cells: a puzzle with many pieces, *Cancer Drug Resist.*, 2022, **5**(4), 850.

74 C. M. Neophytou, *et al.*, Apoptosis deregulation and the development of cancer multi-drug resistance, *Cancers*, 2021, **13**(17), 4363.

75 M. Hassan, *et al.*, Apoptosis and molecular targeting therapy in cancer, *BioMed Res. Int.*, 2014, **2014**, 150845.

76 C. M. Pfeffer and A. T. Singh, Apoptosis: a target for anticancer therapy, *Int. J. Mol. Sci.*, 2018, **19**(2), 448.

77 T. Bezabeh, *et al.*, Detection of drug-induced apoptosis and necrosis in human cervical carcinoma cells using $^1$H NMR spectroscopy, *Cell Death Differ.*, 2001, **8**(3), 219–224.

78 Y. Wang, *et al.*, Cytotoxicity, DNA damage, and apoptosis induced by titanium dioxide nanoparticles in human non-small cell lung cancer A549 cells, *Environ. Sci. Pollut. Res.*, 2015, **22**, 5519–5530.

79 W. Stallaert, *et al.*, The structure of the human cell cycle, *Cell Syst.*, 2022, **13**(3), 230–240.e3.

80 Y. Sun, *et al.*, The influence of cell cycle regulation on chemotherapy, *Int. J. Mol. Sci.*, 2021, **22**(13), 6923.

81 A. E. Eastman and S. Guo, The palette of techniques for cell cycle analysis, *FEBS Lett.*, 2020, **594**(13), 2084–2098.

82 G. I. Shapiro and J. W. Harper, Anticancer drug targets: cell cycle and checkpoint control, *J. Clin. Invest.*, 1999, **104**(12), 1645–1653.

83 D. Plesca, S. Mazumder and A. Almasan, DNA damage response and apoptosis, *Methods Enzymol.*, 2008, **446**, 107–122.

84 T. Kawabe, G2 checkpoint abrogators as anticancer drugs, *Mol. Cancer Ther.*, 2004, **3**(4), 513–519.

85 B.-Y. Peng, *et al.*, AGA induces sub-G1 cell cycle arrest and apoptosis in human colon cancer cells through p53-independent/p53-dependent pathway, *BMC Cancer*, 2023, **23**(1), 1–13.

86 H. Chang, *et al.*, Effect of Titanium Dioxide Nanoparticles on Mammalian Cell Cycle In Vitro: A Systematic Review and Meta-Analysis, *Chem. Res. Toxicol.*, 2022, **35**(9), 1435–1456.

87 J. Karch, *et al.*, Bax and Bak function as the outer membrane component of the mitochondrial permeability pore in regulating necrotic cell death in mice, *eLife*, 2013, **2**, e00772.

88 M. Wang and M. Thanou, Targeting nanoparticles to cancer, *Pharmacol. Res.*, 2010, **62**(2), 90–99.

89 G. Dewson and R. M. Kluck, Mechanisms by which Bak and Bax permeabilise mitochondria during apoptosis, *J. Cell Sci.*, 2009, **122**(16), 2801–2808.

90 C. Garrido, *et al.*, Mechanisms of cytochrome c release from mitochondria, *Cell Death Differ.*, 2006, **13**(9), 1423–1433.

91 A. Peña-Blanco and A. J. García-Sáez, Bax, Bak and beyond—mitochondrial performance in apoptosis, *FEBS J.*, 2018, **285**(3), 416–431.

92 T. T. Renault and J. E. Chipuk, Death upon a kiss: mitochondrial outer membrane composition and organelle communication govern sensitivity to BAK/BAX-dependent apoptosis, *Chem. Biol.*, 2014, **21**(1), 114–123.
93 Z. Xia, *et al.*, Titanium dioxide nanoparticles induce mitochondria-associated apoptosis in HepG2 cells, *RSC Adv.*, 2018, **8**(55), 31764–31776.
94 R. Vigneshwaran, D. Ezhilarasan and S. Rajeshkumar, Inorganic titanium dioxide nanoparticles induces cytotoxicity in colon cancer cells, *Inorg. Chem. Commun.*, 2021, **133**, 108920.
95 Y. Chen, *et al.*, Anticancer efficacy enhancement and attenuation of side effects of doxorubicin with titanium dioxide nanoparticles, *Int. J. Nanomed.*, 2011, 2321–2326.
96 S. A. Lakhani, *et al.*, Caspases 3 and 7: key mediators of mitochondrial events of apoptosis, *Science*, 2006, **311**(5762), 847–851.
97 M. Mubeen and S. G. Kini, A review on the design and development of EGFR tyrosine kinase inhibitors in cancer therapy, *Int. J. Ther. Appl.*, 2012, **5**, 29–37.